Hindawi
Shock and Vibration
Volume 2023, Article ID 9954054, 20 pages
https://doi.org/10.1155/2023/9954054

Research Article

Statistically Optimized Near-Field Acoustic Holography Using Prolate Spheroidal Wave Functions

Xuxin Zhang,[1] **Jingjun Lou**,[2] **Jinfang Lu**,[1] **Ronghua Li**,[1] **and Shijian Zhu**[2]

[1]*College of Power Engineering, Naval University of Engineering, 717 Liberation Avenue, Wuhan 430033, China*
[2]*College of Naval Architecture and Ocean Engineering, Naval University of Engineering, 717 Liberation Avenue, Wuhan 430033, China*

Correspondence should be addressed to Jingjun Lou; 2500896676@qq.com

Received 5 January 2023; Revised 12 June 2023; Accepted 18 August 2023; Published 31 August 2023

Academic Editor: Arcanjo Lenzi

Near-field acoustic holography (NAH) is an effective tool for realizing accurate sound field reconstruction in three-dimensional space on the prerequisite that appropriate elementary wave functions are selected or constructed to match the characteristics of the sound sources. However, for elongated sources, common wave functions, i.e., plane, cylindrical, or spherical waves, sometimes do not perform well during the sound field projections. To solve this problem, statistically optimized near-field acoustical holography combined with prolate spheroidal wave functions is proposed. In the approach, the sound field is expanded by a series of prolate spheroidal wave functions, whose wavefronts can be set nearly conformal to the elongated sources. Based on these wave functions, fewer expansion terms are required to model the sound field, and the need for regularization can be reduced during the inverse solving process. Therefore, the accuracy of the reconstruction results can be further improved. Numerical simulations are conducted by two types of elongated source models, namely, spatially separated and extended. The results show that the proposed method can effectively reconstruct the sound pressures of elongated sources and perform robustly across a wide frequency range. Simultaneously, a designed experiment is carried out in an anechoic chamber, which demonstrates the feasibility of the proposed method.

1. Introduction

Near-field acoustic holography (NAH) [1] is a powerful technique for noise source identification and sound field visualization. It can realize accurate sound field reconstruction in three-dimensional space with a transducer array placed in the near-field of sound sources. Because of the measurement of evanescent waves, the limitation of the Raleigh criterion can be circumvented in NAH [2], and the sound sources can be localized with a high resolution. In general, NAH models a sound field as a superposition of elementary wave functions (EWFs) [3], whose weighting coefficients are calculated by matching sound pressures measured on the hologram surface. The EWFs can be plane, cylindrical, or spherical wave functions, and sound fields generated by monopole, dipole, or multipole point sources in different positions can also be regarded as EWFs [4]. However, NAH is an inverse acoustic problem, which requires not only a regularization procedure but also an appropriate selection or construction of the EWFs to yield stable solutions, especially for sound sources with complex shapes. Once the EWFs match the characteristics of the sound sources well, the ill-posedness of the inverse problem can be suppressed [3], and the reconstruction results can be less sensitive to the measurement noise.

After 40 years of development, various NAH algorithms based on different EWFs have been established, for example, discrete Fourier transform-based NAH (DFT-based NAH) [5–7], inverse boundary element method (IBEM) [8–10], equivalent source method (ESM) [11–14], statistically optimized NAH (SONAH) [15–17], Helmholtz equation least squares (HELS) [18–21], and so on. Theoretically, DFT-based NAH implicitly expands the sound field by a set of EWFs such as plane, cylindrical, or spherical wave functions,

while the spatial spectra can be considered as the weighting coefficients. The advantages of DFT-based NAH are prominent; for instance, it is simple to implement, and the calculation speed is usually very high. However, in DFT-based NAH, the hologram surface and the source surface are constrained to be conformal to the level surface of a separable coordinate system, which cannot always be satisfied in engineering practice. In order to cope with irregularly shaped sound sources, IBEM is developed. It can construct a transfer matrix relating to the radiated sound pressure to the normal component of the surface velocity by discretizing the Helmholtz integral equation directly or by introducing fictitious simple sources on the source surface indirectly [22]. In fact, the fictitious simple sources here play the same roles as the EWFs and are used as an intermediate step to recover the sound field. Since the discretization procedure in IBEM is so complex, ESM is proposed, which is characterized by its simplicity and high efficiency. The basic assumption of ESM is that the sound field radiated by a vibrating structure can be expressed by a set of equivalent sources (monopole or dipole) distributed in the interior of the structure. Generally, the radiated sound fields from these equivalent sources can be regarded as a series of EWFs, and the weighting coefficients (source strengths) are usually solved by satisfying measured pressures on the hologram surface. Different from ESM, SONAH uses a single set or multiple sets of EWFs (plane, cylindrical, or spherical wave functions) to establish a sound field transfer matrix between the hologram locations and the reconstruction locations, while Tikhonov regularization is usually employed to stabilize the reconstruction results [23]. As a similar approach to SONAH, HELS explicitly calculates the coefficients of the EWFs and the errors are minimized by a least squares method (LSM) [24]. Overall, SONAH and HELS can be applied to an arbitrarily shaped sound source and have no restrictions on the positioning of the measurement points. In addition, SONAH and HELS can both be implemented with only a few measurements and yet produce accurate reconstruction results. However, Wang and Wu [18] and Wall et al. [3] pointed out that the EWFs should be carefully selected to match the characteristics of the sound sources or the sound field. For example, the spherical wave functions are often selected for a chunky object, and the plane wave functions are often selected for a rectangular plate. Otherwise, SONAH and HELS may perform a poor convergency because more EWFs are needed during the sound field projection. Once high-order terms are used, noise on the hologram surface can affect the reconstruction results easily.

The fundamentals of the aforementioned NAH algorithms can be concluded as follows: the radiated sound field is approximated by a series of EWFs, whose weighting coefficients are estimated by the measured data. Then, a sound field transfer matrix between the hologram locations and the reconstruction locations is established. Finally, an appropriate regularization method is incorporated to stabilize the reconstruction results. Overall, the performance of different NAH algorithms is mainly influenced by the ability of the EWFs to represent the sound field, the ability of the hologram surface to record enough sound field information, and the ability of the regularization method to filter out the noise contamination [3]. To be more specific, the EWFs can be selected from the eigen functions of the Helmholtz equation in different coordinate systems, such as plane, cylindrical, or spherical wave functions. Typically, these wave functions are orthogonal and complete in the space domain. At the same time, the EWFs can also be constructed by the equivalent sources, but the distribution density and retreat distance from the source surface need to be designed manually. Generally, the EWFs are expected to reflect the geometry of the vibrating body, which can reduce the need for regularization and improve the accuracy of reconstruction results. Therefore, it is important to select or construct proper EWFs according to the characteristics of the sound sources.

The objective of this paper is to reconstruct the radiated sound field of elongated sound sources, such as the unmanned underwater vehicle of large aspect ratios or the trailing edge of airfoils. As a result, prolate spheroidal wave functions (PSWFs) [25] are chosen as a new kind of EWFs in NAH to represent the radiated sound field. It should be noted that PSWFs are the eigen functions of the Helmholtz equation in the prolate spheroidal coordinate system. Of course, PSWFs are orthogonal and complete in the space domain. Besides, for prolate spheroidal waves, the wavefronts are just like a sphere stretched along a certain spatial dimension and can be set nearly conformal to the geometry of the elongated source, which may lead to a strong ability of the PSWFs to represent the radiated sound field. The formulas and characteristics of PSWFs are systematically described by Flammer [25] and Li et al. [26]. Though PSWFs are complex and not easy to calculate, much work has been performed to simplify the calculation procedure and improve the numerical precision, and several reliable code scripts shared by Van Buren and Boisvert [27], Li et al. [28], Falloon et al. [29], Ogburn et al. [30], and Adelman et al. [31] have been proven to be working effectively, which contribute greatly to the application of PSWFs. Up to now, PSWFs have been widely used in many research fields such as electromagnetic scattering [26], acoustic scattering [32], and acoustic radiation modes [33].

In the present work, SONAH combined with PSWFs is proposed to reconstruct the radiated sound field of an elongated sound source. For brevity, the proposed method is abbreviated to PS-SONAH. In this method, the radiated sound field is expanded by a series of PSWFs, and the reconstructed sound pressures are expressed as a linear superposition of the measured sound pressures. Meanwhile, the modified Tikhonov regularization (MTR) method [20] is incorporated to deal with the ill-posed inverse problem, while the regularization parameter is chosen by the generalized cross-validation (GCV) [34] method. The effectiveness and robustness of the proposed method are verified through numerical simulations and a designed experiment, and the advantages of the proposed method for elongated sound sources are demonstrated through a comparison with traditional SONAH algorithms that use plane, cylindrical, or spherical wave functions, representing the sound field. The present study also includes an investigation of the influence

of a key parameter of the proposed method, namely, the interfocal distance.

This paper is organized as follows: in Section II, the basic theory of PS-SONAH is presented. In Section III, numerical simulations are conducted to validate the effectiveness of PS-SONAH and compare the proposed method with traditional SONAH algorithms, and the configuration of the interfocal distance in PS-SONAH is explored. In Section IV, a designed experiment is carried out to validate the feasibility of PS-SONAH. Finally, conclusions are summarized in Section V.

2. Statistically Optimized Near-Field Acoustic Holography Using Prolate Spheroidal Wave Functions

2.1. Prolate Spheroidal Coordinate System. The prolate spheroidal coordinate system can be constructed by rotating the two-dimensional elliptic coordinate system around the major axis of the confocal ellipses [25, 26]. As shown in Figure 1, in a prolate spheroidal coordinate system, the coordinate surfaces are prolate spheroids (ξ = "const"), hyperboloids (η = "const"), and half-planes (φ = "const"). The interfocal distance is denoted by d. The prolate spheroids are formed by rotating the confocal ellipses, and the hyperboloids are formed by rotating the confocal hyperbolas. Similar to the Cartesian, cylindrical, and spherical coordinate systems, the prolate spheroidal coordinate system is also a curvilinear orthogonal system. When the z-axis is chosen as the axis of rotation, prolate spheroidal coordinates (ξ, η, φ) are related to Cartesian coordinates (x, y, z) by the following:

$$\begin{cases} x = \dfrac{d}{2}\sqrt{\left(\xi^2 - 1\right)\left(1 - \eta^2\right)}\cos\varphi, \\ y = \dfrac{d}{2}\sqrt{\left(\xi^2 - 1\right)\left(1 - \eta^2\right)}\sin\varphi, \\ z = \dfrac{d}{2}\xi\eta, \end{cases} \tag{1}$$

where $1 \le \xi < \infty, -1 \le \eta \le 1$, and $0 \le \varphi \le 2\pi$. Correspondingly, coordinates (ξ, η, φ) can be derived from Cartesian coordinates (x, y, z) as follows:

$$\begin{cases} \xi = \dfrac{(R_1 + R_2)}{d}, \\ \eta = \dfrac{(R_1 - R_2)}{d}, \\ \varphi = a\tan2\left(\dfrac{y}{x}\right), \end{cases} \tag{2}$$

where $R_1 = \sqrt{(z + d/2)^2 + x^2 + y^2}$ and $R_2 = \sqrt{(z - d/2)^2 + x^2 + y^2}$ represent the distances between the field point and two foci and $a\tan2(\bullet)$ represents the four-quadrant inverse tangent function.

2.2. Sound Field Expansion by Prolate Spheroidal Wave Functions. The sound pressure radiated from an elongated sound source into the ideal fluid medium should satisfy the wave equation. For a time-independent and single-frequency sound field, the wave equation can be transformed into the Helmholtz equation as follows:

$$\left(\nabla^2 + k^2\right)p(\mathbf{r}) = 0, \tag{3}$$

where $p(\mathbf{r})$ represents the complex sound pressure, $k = \omega/v$ is the wave number, ω is the angular frequency, and v is the sound speed. The Helmholtz equation is separable in the prolate spheroidal coordinate system and can be rewritten as [25]

$$\left[\frac{\partial}{\partial\xi}\left(\xi^2 - 1\right)\frac{\partial}{\partial\xi} + \frac{\partial}{\partial\eta}\left(1 - \eta^2\right)\frac{\partial}{\partial\eta} + \frac{\xi^2 - \eta^2}{\left(\xi^2 - 1\right)\left(1 - \eta^2\right)}\frac{\partial^2}{\partial\varphi^2} + c^2\left(\xi^2 - \eta^2\right)\right]p(\xi, \eta, \varphi) = 0, \tag{4}$$

where $c = kd/2 = \pi d/\lambda$ is a dimensionless quantity reflecting the ratio of d to the wavelength λ. By the separation of variables, the eigen functions to equation (4) are derived as

$$\Phi_{mn}^{(q)}(\xi, \eta, \varphi; c) = R_{mn}^{(q)}(c, \xi)S_{mn}(c, \eta)\begin{cases} \cos(m\varphi), \\ \sin(m\varphi), \end{cases} \tag{5}$$

where $\Phi_{mn}^{(q)}(\xi, \eta, \varphi; c)$ is the primitive PSWFs, $R_{mn}^{(q)}(c, \xi)$ is the q^{th} kind of prolate spheroidal radial function with $q = 1, 2, 3, 4$, and $S_{mn}(c, \eta)$ is the first kind of prolate spheroidal angle function. The subscripts $m = 0, 1, 2, \ldots$ and $n = m, m + 1, m + 2, \ldots$ represent the order and degree of the PSWFs, respectively.

Previous studies have demonstrated the analogous relationships between $R_{mn}^{(q)}(c, \xi)$ and the spherical Bessel functions [28], indicating that $R_{mn}^{(3)}(c, \xi)$ and $R_{mn}^{(4)}(c, \xi)$ can be obtained by $R_{mn}^{(1)}(c, \xi)$ and $R_{mn}^{(2)}(c, \xi)$ in the form as follows:

$$\begin{aligned} R_{mn}^{(3)}(c, \xi) &= R_{mn}^{(1)}(c, \xi) + iR_{mn}^{(2)}(c, \xi), \\ R_{mn}^{(4)}(c, \xi) &= R_{mn}^{(1)}(c, \xi) - iR_{mn}^{(2)}(c, \xi), \end{aligned} \tag{6}$$

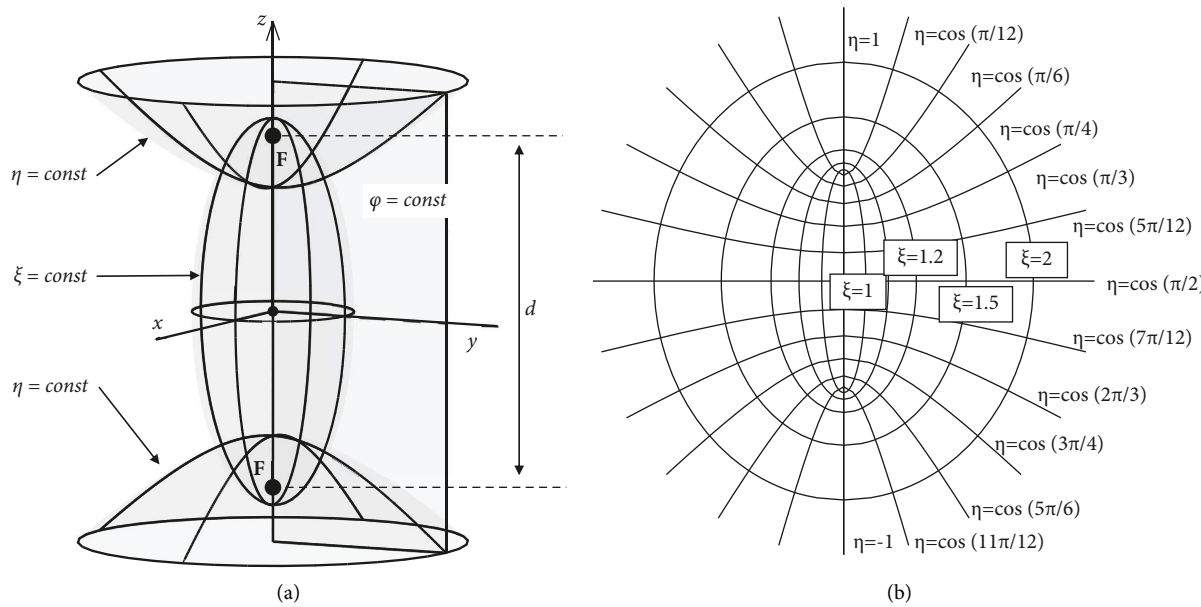

Figure 1: Prolate spheroidal coordinate system: (a) coordinate surfaces and (b) confocal ellipses and hyperbolas. (ξ, η, φ) represents the prolate spheroidal coordinates.

where $i = \sqrt{-1}$ is the imaginary unit. Meanwhile, the asymptotic forms of $R_{mn}^{(3)}(c, \xi)$ and $R_{mn}^{(4)}(c, \xi)$ are given by the following [25]:

$$\lim_{c\xi \longrightarrow \infty} R_{mn}^{(3)}(c, \xi) = \frac{1}{c\xi} \exp\left(\mathrm{i}c\xi - i\frac{(n+1)\pi}{2} \right),$$
$$\lim_{c\xi \longrightarrow \infty} R_{mn}^{(4)}(c, \xi) = \frac{1}{c\xi} \exp\left(-\mathrm{i}c\xi + i\frac{(n+1)\pi}{2} \right). \tag{7}$$

It is observed that both $R_{mn}^{(3)}(c, \xi)$ and $R_{mn}^{(4)}(c, \xi)$ can satisfy the Sommerfeld radiation condition in the far field $(c\xi \longrightarrow \infty)$. When the time dependency is assumed as $e^{-i\omega t}$, $R_{mn}^{(3)}(c, \xi)$ and $R_{mn}^{(4)}(c, \xi)$ can be used to describe the distance dependency of the outgoing and incoming wave functions, respectively [35]. To further depict outgoing and incoming waves in the three-dimensional space, the φ-dependency should be changed from $\cos(m\varphi)$ and $\sin(m\varphi)$ to $e^{\mathrm{i}m\varphi}$. In this case, the negative integers of m must be considered. Therefore, three new sets of functions are defined [25] as follows:

$$R_{-mn}^{(3)}(c, \xi) = R_{mn}^{(3)}(c, \xi),$$
$$R_{-mn}^{(4)}(c, \xi) = R_{mn}^{(4)}(c, \xi),$$
$$S_{-mn}(c, \eta) = (-1)^m \frac{(n-m)!}{(n+m)!} S_{mn}(c, \eta). \tag{8}$$

Notice that these defined functions are important complements to the primitive PSWFs and make it possible to construct the outgoing and incoming wave functions. In the following, the subscripts of $R_{mn}^{(3)}(c, \xi)$, $R_{mn}^{(4)}(c, \xi)$, and $S_{mn}(c, \eta)$ are redefined as $n = 0, 1, \ldots, \infty$ and $m = -n, \ldots, -1, 0, 1, \ldots, n$.

Since the differential equations with respect to $S_{mn}(c, \eta)$ and $e^{im\varphi}$ are in Sturm–Liouville form [30], following the Sturm–Liouville theory, the eigen functions $S_{mn}(c, \eta)$ can form an orthogonal basis over the interval $\eta \in (-1, 1)$, and the eigen functions $e^{im\varphi}$ can form an orthogonal basis over the interval $\varphi \in (0, 2\pi)$. Consequently, it is inferred that the products of $S_{mn}(c, \eta)$ and $e^{im\varphi}$, $S_{\mathrm{mn}}(c, \eta)e^{im\varphi}$, can form an orthogonal basis over the product domain. And the orthogonality property can be expressed by

$$\int_0^{2\pi} \mathrm{d}\varphi \int_{-1}^{1} S_{mn}(c, \eta) e^{im\varphi} \left[S_{m'n'}(c, \eta) e^{im'\varphi} \right]^* \mathrm{d}\eta$$
$$= 2\pi N_{mn} \delta_{mm'} \delta_{nn'}, \tag{9}$$
$$N_{mn} = \frac{2}{2n+1} \frac{(n+m)!}{(n-m)!},$$

where N_{mn} is the normalization factor, $\delta_{nn'}$ and $\delta_{mm'}$ are the Kronecker delta functions, and the superscript "$*$" represents the complex conjugation. Analogous to the spherical harmonics, the prolate spheroidal harmonics can be defined by

$$H_n^m(\eta, \varphi; c) = \sqrt{\frac{2n+1}{4\pi} \frac{(n-m)!}{(n+m)!}} S_{mn}(c, \eta) e^{im\varphi}. \tag{10}$$

Of course, the prolate spheroidal harmonics $H_n^m(\eta, \varphi; c)$ are normalized and orthogonal:

$$\int_0^{2\pi} \mathrm{d}\varphi \int_{-1}^{1} H_n^m(\eta, \varphi; c) H_{n'}^{m'}(\eta, \varphi; c)^* \mathrm{d}\eta = \delta_{mm'} \delta_{nn'}. \tag{11}$$

It should be noted that $H_n^m(\eta,\varphi;c)$ is not orthogonal over the real spheroid surface since the surface area Jacobian (weighting function) is not mentioned in equation (11). Instead, $H_n^m(\eta,\varphi;c)$ is orthogonal over a special spheroid surface with respect to a unit weighting function [33].

When the prolate spheroidal radial functions $R_{mn}^{(3)}(c,\xi)$ and $R_{mn}^{(4)}(c,\xi)$ and the prolate spheroidal harmonics $H_n^m(\eta,\varphi;c)$ are combined, we can express the outgoing and incoming PSWFs as

$$\begin{aligned}\Phi_{mn}^{\text{out}}(\xi,\eta,\varphi;c) &= R_{mn}^{(3)}(c,\xi)H_n^m(\eta,\varphi;c),\\ \Phi_{mn}^{\text{in}}(\xi,\eta,\varphi;c) &= R_{mn}^{(4)}(c,\xi)H_n^m(\eta,\varphi;c).\end{aligned} \tag{12}$$

Evidently, $\Phi_{mn}^{\text{out}}(\xi,\eta,\varphi;c)$ and $\Phi_{mn}^{\text{in}}(\xi,\eta,\varphi;c)$ can form an orthogonal and complete spatial basis, and any steady sound field obeying the Helmholtz equation in a source-free region can be expressed by the outgoing and incoming PSWFs as follows:

$$\begin{aligned}p(\xi,\eta,\varphi) = \sum_{n=0}^{\infty}\sum_{m=-n}^{n}\Big[&a_{mn}(c)\Phi_{mn}^{\text{out}}(\xi,\eta,\varphi;c)\\ &+ b_{mn}(c)\Phi_{mn}^{\text{in}}(\xi,\eta,\varphi;c)\Big],\end{aligned} \tag{13}$$

where $a_{mn}(c)$ and $b_{mn}(c)$ are the undetermined weighting coefficients. However, for an exterior acoustic problem, all the sound sources are within an enclosed boundary surface. The incoming prolate spheroidal waves cannot be excited, and only the outgoing prolate spheroidal waves should be considered. Thus, the coefficients of $\Phi_{mn}^{\text{in}}(\xi,\eta,\varphi;c)$ are set to zero and $b_{mn}(c)=0$, and the solution to the exterior problem can be simplified to

$$p(\xi,\eta,\varphi) = \sum_{n=0}^{\infty}\sum_{m=-n}^{n} a_{\text{mn}}(c)\Phi_{mn}^{\text{out}}(\xi,\eta,\varphi;c). \tag{14}$$

2.3. Principle of Statistically Optimized Near-Field Acoustic Holography. The principle of SONAH is that the sound field can be represented by a set of EWFs, and the reconstructed sound pressure can be calculated as a linear superposition of the measured sound pressures [4, 36]. In this paper, the outgoing PSWFs are introduced to SONAH, and a new sound field reconstruction method called PS-SONAH is established. In fact, PS-SONAH is an extension of the SONAH method. It is assumed that the complex sound pressures are measured at a set of locations, namely, $\mathbf{r}_{hl} = (\xi_{hl},\eta_{hl},\varphi_{hl})$, $l = 1,2,\ldots,L$, and on the hologram surface Γ_h. Since outgoing PSWFs are utilized to approximate the radiated sound field, the pressures on Γ_h can be expanded by the following:

$$p(\mathbf{r}_{hl}) \approx \sum_{j=1}^{J} a_j(c)\Phi_j^{\text{out}}(\mathbf{r}_{hl};c), \tag{15}$$

where the subscripts of the outgoing PSWFs are replaced by $j = n^2+n+m+1$. Compared to equation (14), the expansion terms are truncated at J in equation (15), and only a subset of functions is used to approximate the sound field. This is because the computational resource is always limited, and the high-order terms should also be discarded for their high sensitivity to the measurement noise. In practice, the approximation error in equation (15) is quite small and can even be neglected when J is properly set up. Considering all the measurement points, equation (15) can be written as follows:

$$\begin{bmatrix} p(\mathbf{r}_{h1})\\ p(\mathbf{r}_{h2})\\ \vdots\\ p(\mathbf{r}_{hl})\\ \vdots\\ p(\mathbf{r}_{hL})\end{bmatrix} = \begin{bmatrix} \Phi_1^{\text{out}}(\mathbf{r}_{h1};c) & \Phi_2^{\text{out}}(\mathbf{r}_{h1};c) & \cdots & \Phi_j^{\text{out}}(\mathbf{r}_{h1};c) & \cdots & \Phi_J^{\text{out}}(\mathbf{r}_{h1};c)\\ \Phi_1^{\text{out}}(\mathbf{r}_{h2};c) & \Phi_2^{\text{out}}(\mathbf{r}_{h2};c) & \cdots & \Phi_j^{\text{out}}(\mathbf{r}_{h2};c) & \cdots & \Phi_J^{\text{out}}(\mathbf{r}_{h2};c)\\ \vdots & \vdots & \ddots & \vdots & \ddots & \vdots\\ \Phi_1^{\text{out}}(\mathbf{r}_{hl};c) & \Phi_2^{\text{out}}(\mathbf{r}_{hl};c) & \cdots & \Phi_j^{\text{out}}(\mathbf{r}_{hl};c) & \cdots & \Phi_J^{\text{out}}(\mathbf{r}_{hl};c)\\ \vdots & \vdots & \ddots & \vdots & \ddots & \vdots\\ \Phi_1^{\text{out}}(\mathbf{r}_{hL};c) & \Phi_2^{\text{out}}(\mathbf{r}_{hL};c) & \cdots & \Phi_j^{\text{out}}(\mathbf{r}_{hL};c) & \cdots & \Phi_J^{\text{out}}(\mathbf{r}_{hL};c)\end{bmatrix}\begin{bmatrix} a_1(c)\\ a_2(c)\\ \vdots\\ a_j(c)\\ \vdots\\ a_J(c)\end{bmatrix}. \tag{16}$$

For the sake of brevity, equation (16) is denoted in matrix form as follows:

$$\mathbf{p}_h = \mathbf{\Psi}_h\mathbf{a}, \tag{17}$$

where $\mathbf{p}_h$ is a column vector of the measured pressures, $\mathbf{a}$ is a column vector of the weighting coefficients, and $\mathbf{\Psi}_h$ is a $L\times J$ matrix of the outgoing PSWFs evaluated at the measurement points.

Furthermore, in SONAH, the sound pressure at an arbitrary reconstruction location $\mathbf{r}_s$ in the source-free region can be estimated by measured sound pressures as follows:

$$p(\mathbf{r}_s) = \sum_{l=1}^{L} g_l(\mathbf{r}_s)p(\mathbf{r}_{\text{hl}}) = \mathbf{p}_h^T\mathbf{g}(\mathbf{r}_s), \tag{18}$$

where $\mathbf{g}(\mathbf{r}_s) = [g_1(\mathbf{r}_s), g_2(\mathbf{r}_s),\ldots,g_L(\mathbf{r}_s)]^T$ is the complex estimation weights and the superscript "T" represents the transpose of a matrix or vector. Generally, $\mathbf{g}(\mathbf{r}_s)$ can be

found by using equation (18) to provide a good estimation for the outgoing PSWFs as follows:

$$\Phi_j^{\text{out}}(\mathbf{r}_s;c)=\sum_{l=1}^{L} g_l(\mathbf{r}_s)\Phi_j^{\text{out}}(\mathbf{r}_{hl};c). \tag{19}$$

Considering different orders, the matrix form of equation (19) can be written as follows:

$$\boldsymbol{\alpha}(\mathbf{r}_s;c)=\mathbf{A}\mathbf{g}(\mathbf{r}_s), \tag{20}$$

where $\boldsymbol{\alpha}(\mathbf{r}_s;c)=[\Phi_1^{\text{out}}(\mathbf{r}_s;c),\Phi_2^{\text{out}}(\mathbf{r}_s;c),\ldots,\Phi_J^{\text{out}}(\mathbf{r}_s;c)]^T$ is a column vector of the outgoing PSWFs evaluated at the position $\mathbf{r}_s$ and $\mathbf{A}$ is the transpose of the matrix $\boldsymbol{\Psi}_h$. The problem of solving equation (20) is overdetermined when the measurement points are less than the wave functions $L<J$. This means that the exact solution does not exist, and only the least square solution can be obtained as follows:

$$\mathbf{g}(\mathbf{r}_s)=\left(\mathbf{A}^H\mathbf{A}\right)^{-1}\mathbf{A}^H\boldsymbol{\alpha}(\mathbf{r}_s;c), \tag{21}$$

where "H" represents the Hermitian transpose and $(\bullet)^{-1}$ represents the pseudoinverse. If $L>J$, the problem of solving equation (20) becomes underdetermined and there are an infinite number of solutions. Among all these solutions, the least-norm solution can be derived as follows:

$$\mathbf{g}(\mathbf{r}_s)=\mathbf{A}^H\left(\mathbf{A}\mathbf{A}^H\right)^{-1}\boldsymbol{\alpha}(\mathbf{r}_s;c). \tag{22}$$

Here, we assume that the sound field is sufficiently measured and the number of measurement points is greater than the number of wave functions. By substituting equation (22) into equation (18), we can get the reconstructed sound pressure as follows:

$$p(\mathbf{r}_s)=\mathbf{p}_h^T\mathbf{A}^H\left(\mathbf{A}\mathbf{A}^H\right)^{-1}\boldsymbol{\alpha}(\mathbf{r}_s;c). \tag{23}$$

Since the matrix $\mathbf{A}\mathbf{A}^H$ is often ill-conditioned, the measurement noise in $\mathbf{p}_h$ can be greatly amplified during the inverse solving process and will easily ruin the reconstruction results; thus, a regularized inverse of $\mathbf{A}\mathbf{A}^H$ is required. As $\mathbf{A}\mathbf{A}^H$ is a positive semidefinite matrix, it can be represented by the eigenvalue expansion as follows:

$$\begin{aligned}\mathbf{A}\mathbf{A}^H&=\mathbf{V}\mathbf{G}\mathbf{V}^H,\\ \mathbf{G}&=\operatorname{diag}\left(\sigma_1,\sigma_2,\ldots,\sigma_j,\ldots,\sigma_J\right),\end{aligned} \tag{24}$$

where $\mathbf{V}$ is a matrix of eigenvectors and $\mathbf{G}$ is a diagonal matrix containing the eigenvalues $\sigma_1>\sigma_2>\ldots>\sigma_J\geq 0$. According to the theory of MTR [37], the regularized inverse of $\mathbf{A}\mathbf{A}^H$ can be expressed by the following:

$$\begin{aligned}\mathbf{R}_\alpha&=\mathbf{V}\mathbf{F}^\alpha\operatorname{diag}\left(\frac{1}{\sigma_1},\frac{1}{\sigma_2},\ldots,\frac{1}{\sigma_J}\right)\mathbf{V}^H,\\ \mathbf{F}^\alpha&\equiv\operatorname{diag}\left(\cdots,\frac{\left|\sigma_j\right|^2}{\left(\left|\sigma_j\right|^2+\alpha\left[\alpha/\left(\alpha+\left|\sigma_j\right|^2\right)\right]^2\right)},\cdots\right),\end{aligned} \tag{25}$$

where α is the regularization parameter and $\mathbf{F}^\alpha$ is a low-pass filter that can alleviate the singularity of small eigenvalues during the matrix inversion. At last, the reconstructed sound pressure can be expressed by the following:

$$p(\mathbf{r}_s)=\mathbf{p}_h^{\mathrm{T}}\mathbf{A}^H\mathbf{R}_\alpha\boldsymbol{\alpha}(\mathbf{r}_s;c). \tag{26}$$

In fact, the accuracy of the reconstructed sound pressure depends heavily on the regularization parameter α. If the regularization parameter is set too large, it will be over-regularized and the main components of the sound field may be filtered out. Instead, when the regularization parameter is too small, it will be under-regularized and the noise influence cannot be effectively suppressed. Hence, in this paper, as Williams [37] suggested, we would find the optimal regularization parameter by minimizing the GCV function as follows:

$$\Lambda(\alpha)\equiv\frac{\left\|\mathbf{p}_h^{\mathrm{T}}\mathbf{A}^H\mathbf{V}\left(\mathbf{E}-\mathbf{F}^\alpha\right)\right\|_2^2}{\left[\operatorname{Tr}\left(\mathbf{E}-\mathbf{F}^\alpha\right)\right]^2}, \tag{27}$$

where $\mathbf{E}$ is the unit matrix, $\|\bullet\|_2$ represents the l_2-norm of a matrix, and $\operatorname{Tr}(\bullet)$ represents the trace of a matrix.

3. Numerical Simulations

The performance of the PS-SONAH method is investigated by two elongated numerical source models, namely, line-array monopoles and a simply supported thin plate driven by a harmonic point force in the center. The line-array monopoles represent the spatially separated sources, and the thin plate represents the spatially extended sources. The two different kinds of source models can validate the effectiveness of PS-SONAH in different circumstances.

The simulation diagram is shown in Figure 2. It can be seen that the measurement configurations for both source models are identical. In the simulations, the source model is located at the plane of $x=0$ m. The hologram surface Γ_h is located at $x=0.2$ m with a dimension of 1.2×1.2 m^2. The pressure measurements are implemented by a planar array containing $25\times 25=625$ microphones. These microphones are spaced uniformly with a resolution of 0.05 m. Note that the dense sampling measurements and the large hologram aperture can make sure that the sound field information is sufficiently recorded. The sound field reconstruction is carried out on three planar surfaces, namely, Γ_1, Γ_2, and Γ_3. These reconstruction surfaces are mutually orthogonal and can reflect the reconstruction results in three-dimensional space. The surface Γ_1 possesses the same size as the hologram surface Γ_h and is located at $x=0.1$ m. The surface Γ_2 is located at $y=0$ m with a dimension of 1.2×0.5 m^2. The surface Γ_3 is located at $z=0$ m with a dimension of 0.5×0.5 m^2. The reconstruction points on the three reconstruction surfaces are all spaced at 0.05 m. At the same time, the intersections of the orthogonal reconstruction surfaces, lines 1–3, are used to investigate the detailed reconstruction results. In particular, line 1 is located at $(x,y)=(0,0)$ m, line 2 is located at $(x,z)=(0,0)$ m, and line 3 is located at $(y,z)=(0,0)$ m.

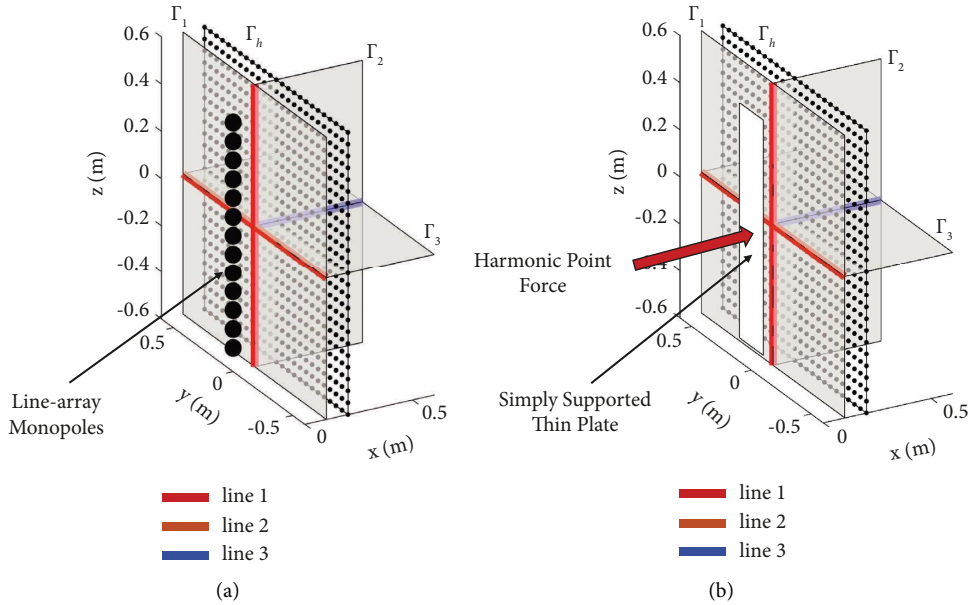

Figure 2: Diagram of two source models: (a) line-array monopoles and (b) a simply supported thin plate driven by a harmonic point force in the center. Γ_h is the hologram surface. Γ_1, Γ_2, and Γ_3 are three reconstruction surfaces. Lines 1–3 are used to investigate the detailed reconstruction results in three different directions.

For comparison, traditional SONAH algorithms that use plane, cylindrical, or spherical wave functions representing the sound field are also conducted. Table 1 lists the four kinds of wave functions that are used in the simulations. In the table, the spherical wave functions that represent outgoing waves are defined as $\Phi^s_{mn}(r,\theta,\varphi)$ with respect to spherical coordinates (r,θ,φ). $h^{(1)}_n(\mathrm{kr})$ is the n^{th}-order spherical Hankel function of the first kind. $Y^m_n(\theta,\varphi)$ is the spherical harmonics of degree n and order m. Meanwhile, the outgoing PSWFs are denoted by $\Phi^{\mathrm{ps}}_{\mathrm{mn}}(\xi,\eta,\varphi;c)$, and the interfocal distance is set to be $d = 1.2\,\mathrm{m}$, slightly larger than the length of the source model. The cylindrical wave functions representing the outgoing waves are denoted by $\Phi^c_{n,k_z}(\rho,\varphi,z)$ with respect to cylindrical coordinates (ρ,φ,z). $H^{(1)}_n(k_r\rho)$ is the n^{th}-order Hankel function of the first kind, k_r is the radial wavenumber, and ρ_0 is a small reference radius. The plane wave functions are defined by $\Phi^p_{k_y,k_z}(x,y,z)$, in which k_x, k_y, and k_z represent the wavenumbers in three axial directions. $F(k_x)$ is a weighting function that is used to ensure a constant directional power density [36]. For the sake of simplicity, traditional SONAH algorithms that use plane, cylindrical, and spherical wave functions representing the sound field are abbreviated as P-SONAH, C-SONAH, and S-SONAH, respectively. In addition, the regularization methods in these three algorithms are set in common with the PS-SONAH method.

The simulation procedure is stated as follows: first, the source model is configured. Then, the theoretical pressures on the hologram surface and three reconstruction surfaces are calculated. In order to model the real testing environment, Gaussian white noise with a signal-to-noise ratio (SNR) of 30 dB is added to the pressures on the hologram surface. Next, pressures on the hologram surface are utilized by different SONAH algorithms to reconstruct the pressures on Γ_1, Γ_2, and Γ_3. Finally, reconstructed pressures are compared to theoretical pressures, and the performances of different SONAH algorithms can be evaluated. To quantitatively assess the performance, the reconstruction error is defined as follows:

Table 1: Four kinds of wave functions used in the simulations.

Spherical wave functions
$\Phi^s_{\mathrm{mn}}(r,\theta,\varphi) = h^{(1)}_n(\mathrm{kr})Y^m_n(\theta,\varphi)$
$n = 0,1,\ldots,10$
$m = -n,-(n-1),\ldots,n-1,n$
Prolate spheroidal wave functions
$\Phi^{\mathrm{ps}}_{mn}(\xi,\eta,\varphi;c) = R^{(3)}_{mn}(c,\xi)H^m_n(\eta,\varphi;c)$
$d = 1.2\,\mathrm{m}$, $c = 1/2kd$
$n = 0,1,\ldots,10$
$m = -n,-(n-1),\ldots,n-1,n$
Cylindrical wave functions
$\Phi^c_{n,k_z}(\rho,\varphi,z) = H^{(1)}_n(k_r\rho)/H^{(1)}_n(k_r\rho_0)e^{in\varphi}e^{ik_zz}$
$k_r = \begin{cases} \sqrt{k^2-k_z^2}, k^2 > k_z^2 \\ i\sqrt{k_z^2-k^2}, k^2 < k_z^2 \end{cases}$
$\rho_0 = 0.02\,\mathrm{m}$
$n = -9,-8,\ldots,-1,0,1,\ldots,8,9$
$\lvert k_z\rvert_{\max} = \pi/0.1\,\mathrm{m}^{-1}$, $\Delta k_z = \frac{2\pi}{2.4}\,\mathrm{m}^{-1}$
Plane wave functions
$\Phi^p_{k_y,k_z}(x,y,z) = F(k_x)e^{i(k_yy+k_zz+k_xx)}$
$k_x = \begin{cases} \sqrt{k^2-k_y^2-k_z^2}, k^2 > k_y^2+k_z^2 \\ i\sqrt{k_y^2+k_z^2-k^2}, k^2 < k_y^2+k_z^2 \end{cases}$
$\mathrm{F}(k_x) = \sqrt{k/\lvert k_x\rvert}$
$\lvert k_y\rvert_{\max} = \pi/0.1\,\mathrm{m}^{-1}$, $\Delta k_y = 2\pi/2.4\,\mathrm{m}^{-1}$
$\lvert k_z\rvert_{\max} = \pi/0.1\,\mathrm{m}^{-1}$, $\Delta k_z = 2\pi/2.4\,\mathrm{m}^{-1}$

$$\mathrm{RE} = \frac{\left\|\mathbf{p}_{cal} - \mathbf{p}_{the}\right\|_2}{\left\|\mathbf{p}_{the}\right\|_2} \times 100\%, \tag{28}$$

where $\mathbf{p}_{cal}$ is the reconstructed pressure and $\mathbf{p}_{the}$ is the theoretical pressure.

3.1. Validation by Line-Array Monopoles. In this section, the performance of PS-SONAH is examined by a line-array source model. As shown in Figure 2(a), the line-array source model consisting of 51 monopoles is placed along the z-axis, spanning from $z = -0.5$ to 0.5 m. The monopoles are spaced at 0.02 m. In the simulation, all the source strengths and phases are set in common. The fluid medium is assumed to be air, and the sound speed is set at 340 m/s. The theoretical sound pressures from the line-array monopoles are all calculated with the free-field Green's function, and the simulation test is conducted at 1000 Hz. After adding the Gaussian white noise, sound pressures on the hologram surface are shown in Figure 3(a). It can be seen that sound fields radiated by different monopoles are joined together because of the strong interference effect. The benchmark pressures on Γ_1, Γ_2, and Γ_3 are also depicted in Figure 3(b).

Since the line-array source model is a highly non-spherical object, Wu [24] suggested that the origin of the spherical wave functions should be backward from the center of the source model by about half of the characteristic dimension. Therefore, we set the origin of spherical wave functions at $(-0.5, 0, 0)$ m. However, for the other three wave functions, the origins of wave functions are still located at the center of the source model. More detailed configurations of the four wave functions are listed in Table 1.

Figure 4 shows the reconstructed pressures by S-SONAH, PS-SONAH, C-SONAH, and P-SONAH and the benchmarks on the surface Γ_1. It can be seen that the reconstructed sound pressures by PS-SONAH and C-SONAH match the benchmark pressures fairly well. In contrast, redundant ripples in Figure 4(e) indicate that P-SONAH does not work well. A possible explanation for this might be that a few high-order plane wave functions (evanescent waves) are incorporated to approximate the interference pattern on Γ_h, but the measurement noise prevents us from getting the right weighting coefficients. Since the amplitudes of these high-order wave functions are greatly amplified during the inverse reconstruction, ripples connected with these functions start to appear on Γ_1 and cause large reconstruction errors. In other words, plane wave functions may not be a good choice to represent the radiated sound field of line-array monopoles, and it is difficult for the regularization method to balance the approximation error on Γ_h and the reconstruction error on Γ_1. For S-SONAH, the reconstructed pressures manifest a radial pattern in Figure 4(b), which can be attributed to the singularity of the spherical wave functions at the locations close to the origin. RE*s* of S-SONAH, PS-SONAH, C-SONAH, and P-SONAH are 24.1%, 2.0%, 2.5%, and 24.2%, respectively. Apparently, the results demonstrate that C-SONAH and PS-SONAH can backward reconstruct the sound field of line-array monopoles well.

Figure 5 depicts a comparison of the reconstructed pressures by S-SONAH, PS-SONAH, C-SONAH, and P-SONAH on surface Γ_2. Figure 6 demonstrates the comparison on surface Γ_3. It is found that S-SONAH, PS-SONAH, and C-SONAH can yield accurate results on both Γ_2 and Γ_3. However, the reconstructed pressures by P-SONAH differ from the benchmarks considerably at locations far from the hologram surface. Moreover, RE*s* of both PS-SONAH and C-SONAH are calculated below 3% on Γ_2 and Γ_3, indicating the effectiveness of PS-SONAH and C-SONAH during the forward sound field reconstruction for line-array monopoles.

To investigate the reconstruction results in a more detailed sense, the sound pressure levels (SPLs) calculated by S-SONAH, PS-SONAH, C-SONAH, and P-SONAH over lines 1–3 are shown in Figure 7. It can be observed that the reconstructed SPLs by S-SONAH differ greatly from the benchmarks at the edges of line 1 and line 2. Meanwhile, P-SONAH presents many ripples over line 2 and displays a huge deviation from the benchmarks over line 3. As explained above, the ability of either plane wave functions or spherical wave functions to represent the sound field of the line-array source model seems inadequate. On the one hand, more expansion terms are required in P-SONAH and S-SONAH to match the pressures on Γ_h. On the other hand, the incorporation of high-order wave functions will make the transfer matrix more sensitive, resulting in too much burden on the regularization method during the inverse solving process. In contrast, PS-SONAH and C-SONAH display almost perfect agreements with the benchmarks over the three lines, which means that both methods can accurately recover the sound field characteristics in three-dimensional space.

Figure 8 shows RE*s* of S-SONAH, PS-SONAH, C-SONAH, and P-SONAH versus frequency on three reconstruction surfaces. The frequency ranges from 100 to 1000 Hz. Obviously, RE*s* of S-SONAH grow larger with the increase of frequency on three reconstruction surfaces, while PS-SONAH can always keep the errors at a low level. Compared to PS-SONAH, there are more fluctuations in the error curves of C-SONAH on Γ_2 and Γ_3, which may be caused by the improper selection of the regularization parameter. Considering the good performance of C-SONAH on Γ_1, it is inferred that the regularization parameter, which is suitable for the sound field reconstruction on Γ_1, may perform over-regularized during the forward sound field projection on Γ_2 and Γ_3. On surface Γ_1, the mean RE*s* of S-SONAH, PS-SONAH, C-SONAH, and P-SONAH in the whole frequency range are 8.5%, 1.7%, 2.9%, and 21.0%, respectively. On surface Γ_2, the mean RE*s* of S-SONAH, PS-SONAH, and C-SONAH is 5.4%, 1.4%, and 3.9%, respectively. On surface Γ_3, the mean RE*s* of S-SONAH, PS-SONAH, and C-SONAH is 3.4%, 0.8%, and 2.0%, respectively. It is evident that the PS-SONAH method has the lowest mean reconstruction errors in the whole frequency range on three reconstruction surfaces, which demonstrates the robustness and superiority of the proposed method for line-array monopoles.

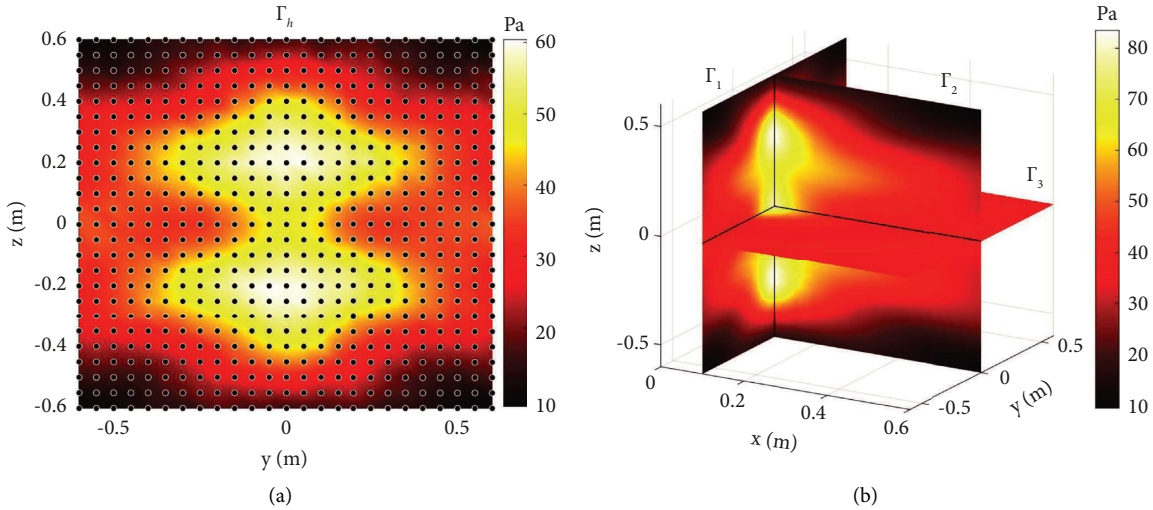

Figure 3: (a) Sound pressures radiated by line-array monopoles on the hologram surface Γ_h with SNR = 30 dB at 1000 Hz. The dots represent the sampling measurements. (b) Benchmark sound pressures on three reconstruction surfaces Γ_1, Γ_2, and Γ_3.

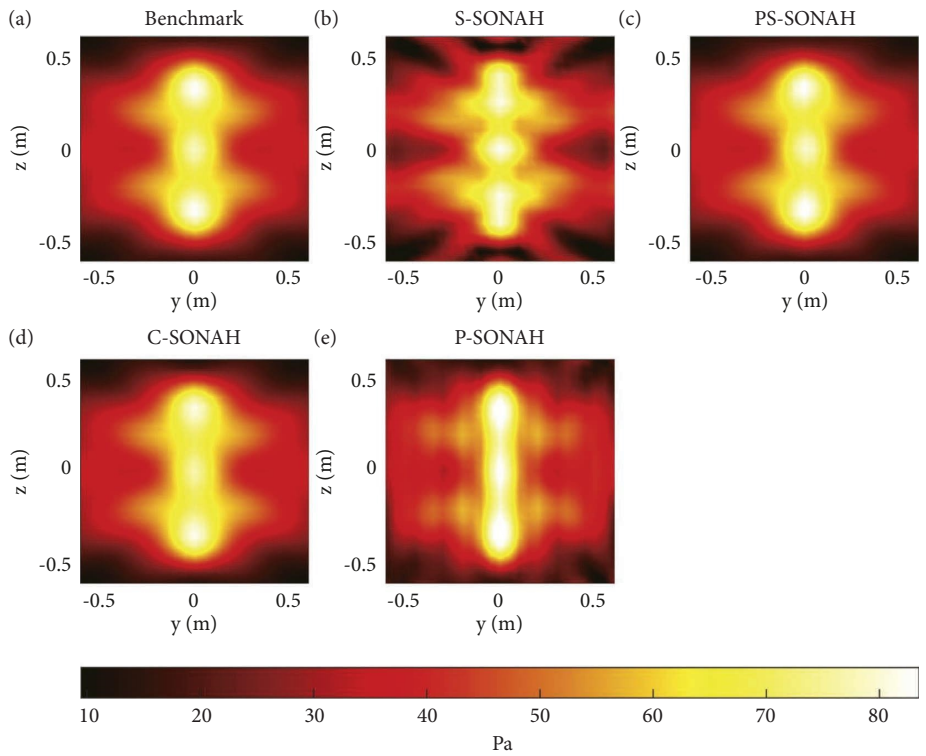

Figure 4: A comparison of the reconstructed pressures at 1000 Hz by S-SONAH, PS-SONAH, C-SONAH, and P-SONAH and the benchmark pressures on the reconstruction surface Γ_1 in terms of line-array monopoles.

3.2. Validation by a Simply Supported Thin Plate. In this section, we validate the PS-SONAH method by a simply supported thin plate. As shown in Figure 2(b), the plate lies in the *yz* plane and is centered at the origin of the coordinate system. The size of the plate is $1.0 \times 0.2\ \mathrm{m}^2$. The length-width ratio of the plate equals 5, indicating that the plate is an elongated sound source. The thickness of the plate is 0.0016 m. Besides, the plate has Young's modulus of 200 GPa. Poisson's ratio is set to 0.28, and the density is set to $7850\ \mathrm{kg/m}^3$. In the simulation, the plate is driven by a harmonic point source of amplitude $F = 1$ N applied at the center, and the simulation is conducted at 1000 Hz, while the sound speed is set at 340 m/s. The measurement configurations are identical to the line-array source model. The amplitude of the normal velocity on the thin plate is given in Figure 9(a). Subsequently, the radiated sound field of the plate is calculated by Rayleigh's integral under free-field conditions [1]. After adding the Gause white noise, the

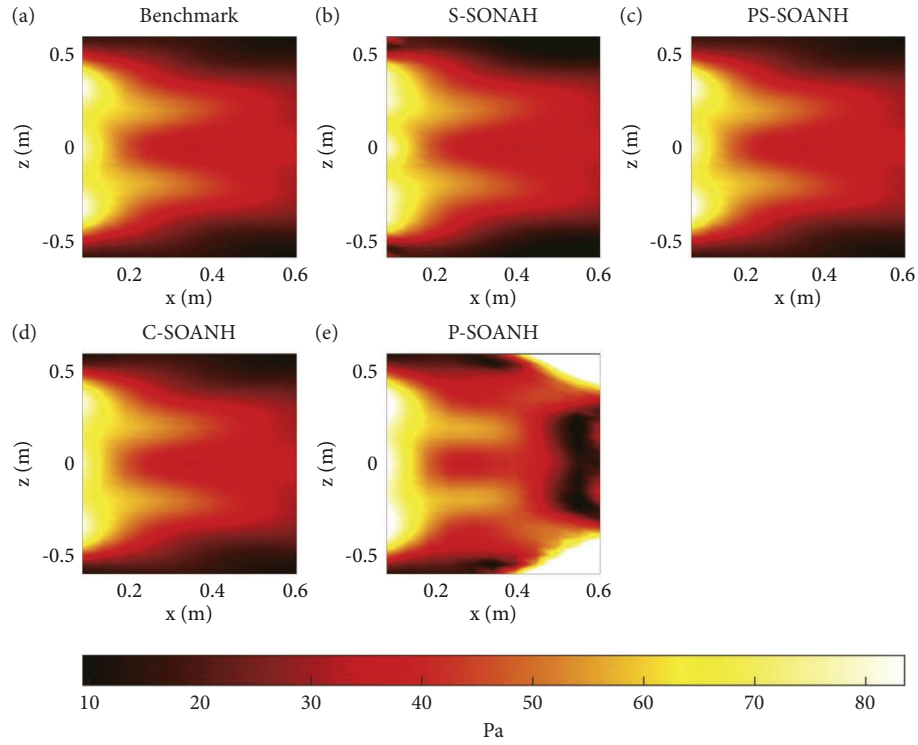

Figure 5: A comparison of the reconstructed pressures at 1000 Hz by S-SONAH, PS-SONAH, C-SONAH, and P-SONAH and the benchmark pressures on the reconstruction surface Γ_2 in terms of line-array monopoles.

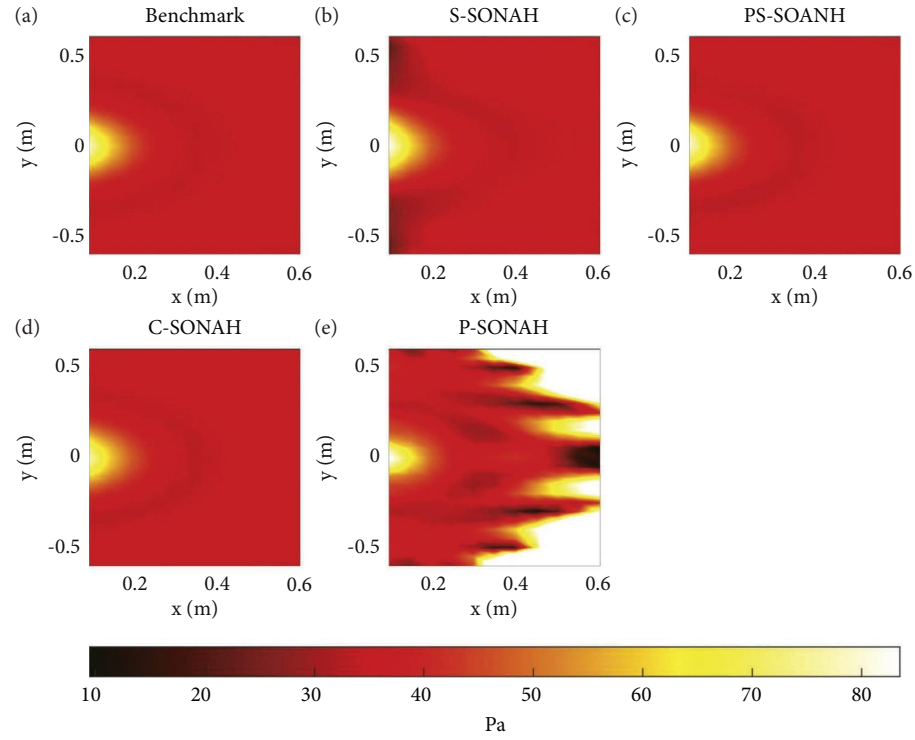

Figure 6: Comparison of the reconstructed pressures at 1000 Hz by S-SONAH, PS-SONAH, C-SONAH, and P-SONAH and the benchmark pressures on the reconstruction surface Γ_3 in terms of line-array monopoles.

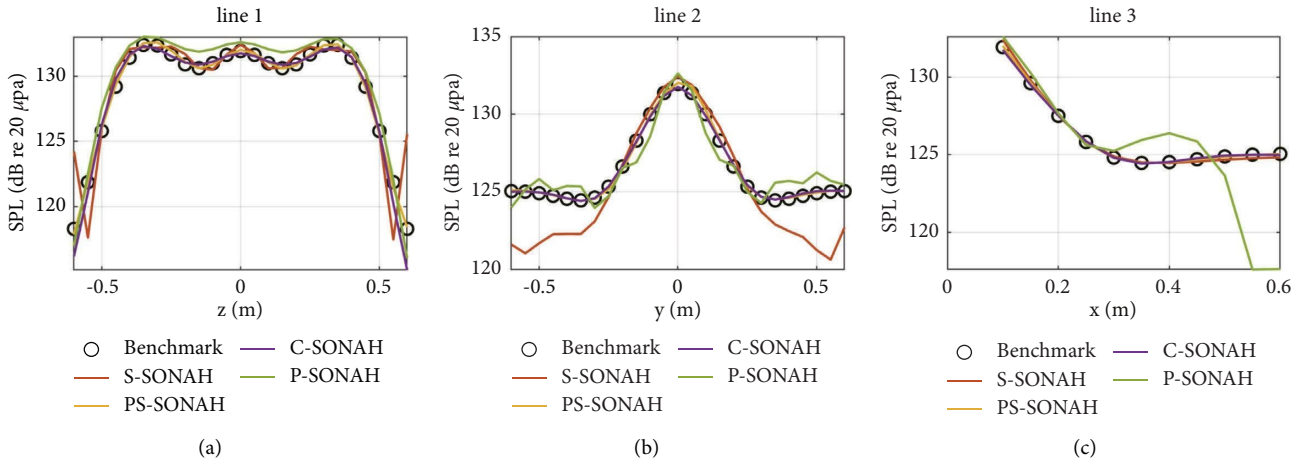

Figure 7: A comparison of the reconstructed SPLs at 1000 Hz by S-SONAH, PS-SONAH, C-SONAH, and P-SONAH and the benchmark SPLs over lines 1–3 in terms of line-array monopoles.

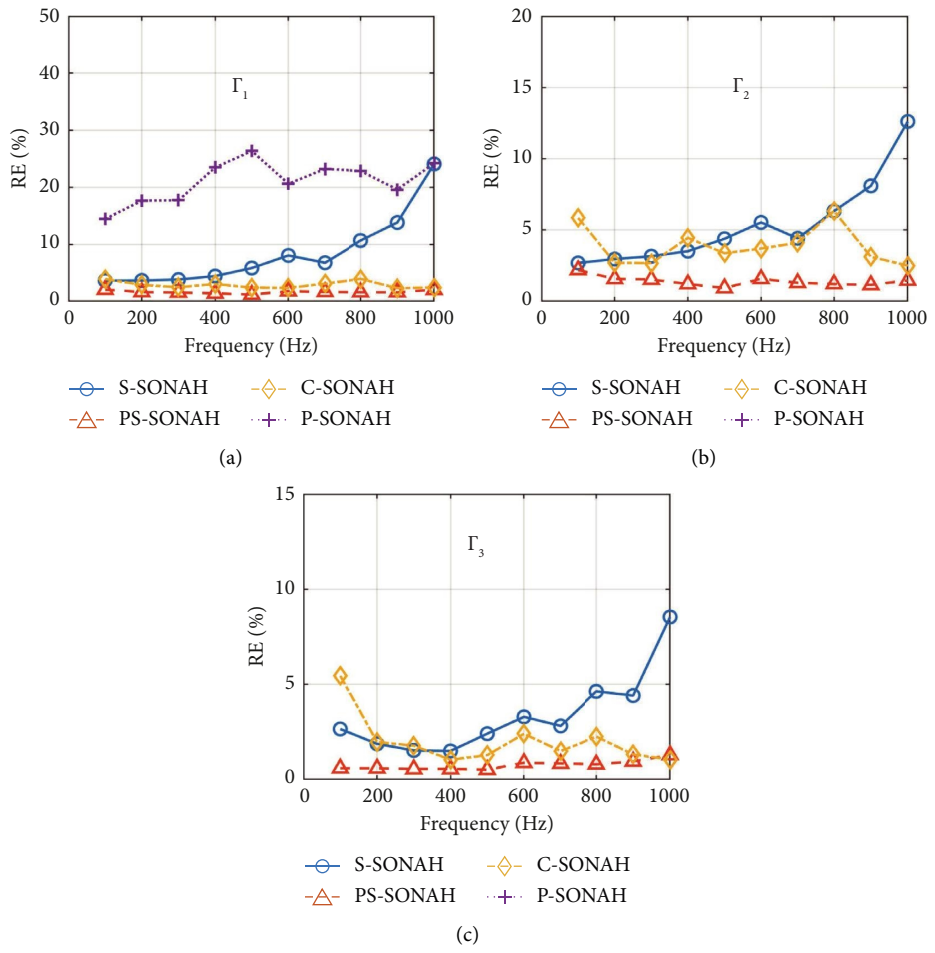

Figure 8: Reconstruction errors of S-SONAH, PS-SONAH, C-SONAH, and P-SONAH on three reconstruction surfaces versus frequency in terms of line-array monopoles.

sound pressures on the hologram surface Γ_h are illustrated in Figure 9(b), and the benchmarks on Γ_1, Γ_2, and Γ_3 are depicted in Figure 9(c).

Similar to the previous numerical experiment, we set the origin of spherical wave functions at $(-0.5, 0, 0)$ m again. And the reconstructed pressures by S-SONAH, PS-SONAH,

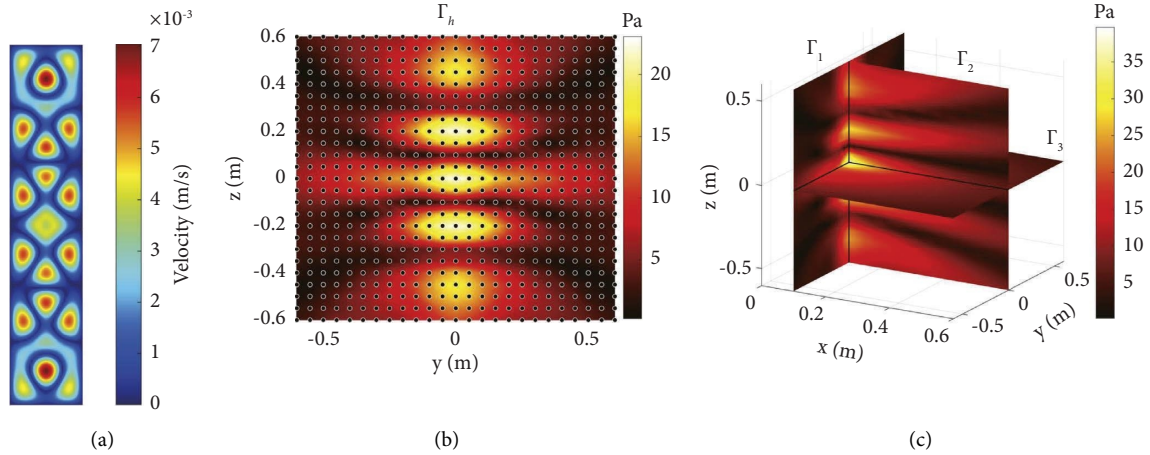

FIGURE 9: (a) The amplitude of the normal velocity on the thin plate at 1000 Hz. (b) Sound pressures on the hologram surface Γ_h with SNR = 30 dB at 1000 Hz. The dots represent the sampling measurements. (c) Benchmark sound pressures on three reconstruction surfaces Γ_1, Γ_2, and Γ_3.

C-SONAH, and P-SONAH and the benchmarks on the three reconstruction surfaces are given in Figures 10–12. It can be seen that all the four SONAH algorithms can give visually similar patterns to the benchmarks on surface Γ_1. However, there are some distortions in the reconstructed pressures by C-SONAH and P-SONAH on surface Γ_2. Meanwhile, the maximum pressure on surface Γ_3 is underestimated apparently by P-SONAH. For a more detailed investigation, reconstructed SPLs and the benchmarks over lines 1–3 are provided in Figure 13. It can be found that the reconstructed SPLs by PS-SONAH and S-SONAH agree with the benchmarks well over lines 1–3. What is surprising is that the spherical wave functions perform a good capability to represent the sound field for such a highly nonspherical source. However, C-SONAH and P-SONAH present large deviations over line 3 and the peak SPLs in line 1 and line 2 are underestimated by P-SONAH. Since the four SONAH algorithms hold the same input data, regularization method, and regularization parameter optimization method, it is reasonable to relate the reconstruction performance to the ability of the wave functions directly. Thus, for the elongated thin plate, cylindrical wave functions and plane wave functions may not perform as well as the other two wave functions. Perhaps more measurements are needed in P-SONAH and C-SONAH to reduce the capacity gap.

To quantitively compare the four algorithms, we can calculate RE*s* of the four SONAH algorithms. RE*s* of S-SONAH, PS-SONAH, C-SONAH, and P-SONAH on surface Γ_1 are 45.9%, 15.9%, 29.1%, and 46.3%, respectively. On surface Γ_2, RE*s* of S-SONAH and PS-SONAH are 20.9% and 8.5%, respectively. On surface Γ_3, RE*s* of S-SONAH and PS-SONAH are 10.9% and 7.3%, respectively. Evidently, PS-SONAH has the most accurate reconstruction results for the elongated thin plate, which demonstrates the effectiveness of the proposed method.

Figure 14 shows the reconstruction errors of S-SONAH, PS-SONAH, C-SONAH, and P-SONAH on three reconstruction surfaces in the frequency range of 100–1000 Hz. On the three surfaces, PS-SONAH and S-SONAH hold similar error curves. By contrast, C-SONAH displays larger errors at 300, 400, and 1000 Hz, which may be related to the failure of the regularization procedure. In this case, it can be inferred that C-SONAH may perform sensitively at these frequencies, and it is not easy for the regularization method to suppress the ill-posedness in C-SONAH. On surface Γ_1, the mean RE*s* of S-SONAH, PS-SONAH, C-SONAH, and P-SONAH are 12.9%, 7.9%, 15.6%, and 34.0%, respectively. On surface Γ_2, the mean RE*s* of S-SONAH, PS-SONAH, and C-SONAH are 8.3%, 6.8%, and 31.1%, respectively. On the surface Γ_3, the mean RE*s* of S-SONAH, PS-SONAH, and C-SONAH are 5.0%, 3.8%, and 20.5%, respectively. Overall, the calculated mean reconstruction errors indicate that PS-SONAH is more robust than the other three SONAH algorithms for the elongated thin plate.

Through the above investigations, the reconstructed pressures of two numerical source models on three reconstruction surfaces and three special lines are presented, and the performances of four SONAH algorithms are compared. It is demonstrated that PS-SONAH can effectively reconstruct the sound pressure of elongated sources in three-dimensional space and holds a more robust reconstruction result than other traditional SONAH algorithms across the frequency range of 100–1000 Hz. In particular, PS-SONAH really shows better performance for spatially separated sources (see Figure 8). As for spatially extended sources, the lead of the proposed method over S-SONAH seems not very prominent (see Figure 14). However, considering the bad behavior of S-SONAH for spatially separated sources, the superiority and robustness of PS-SONAH for different kinds of elongated sources can be found easily.

3.3. Effect of the Interfocal Distance d. In the above simulations of the proposed method, the interfocal distance is directly set to $d = 1.2$ m, which is slightly larger than the

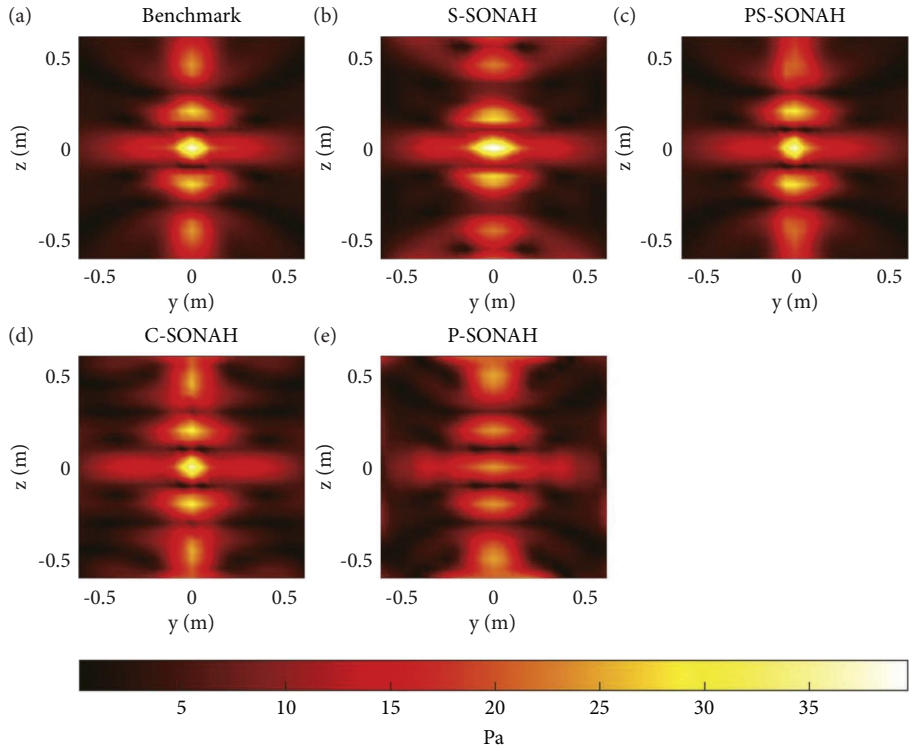

Figure 10: A comparison of the reconstructed pressures at 1000 Hz by S-SONAH, PS-SONAH, C-SONAH, and P-SONAH and the benchmark pressures on the reconstruction surface Γ_1 in terms of a simply supported thin plate.

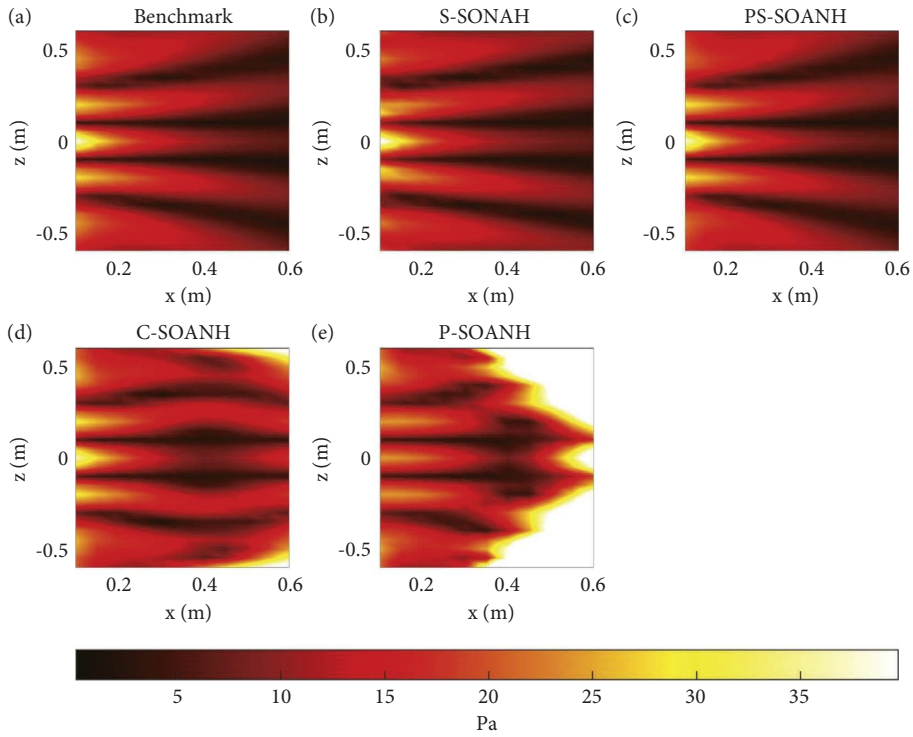

Figure 11: A comparison of the reconstructed pressures at 1000 Hz by S-SONAH, PS-SONAH, C-SONAH, and P-SONAH and the benchmark pressures on the reconstruction surface Γ_2 in terms of a simply supported thin plate.

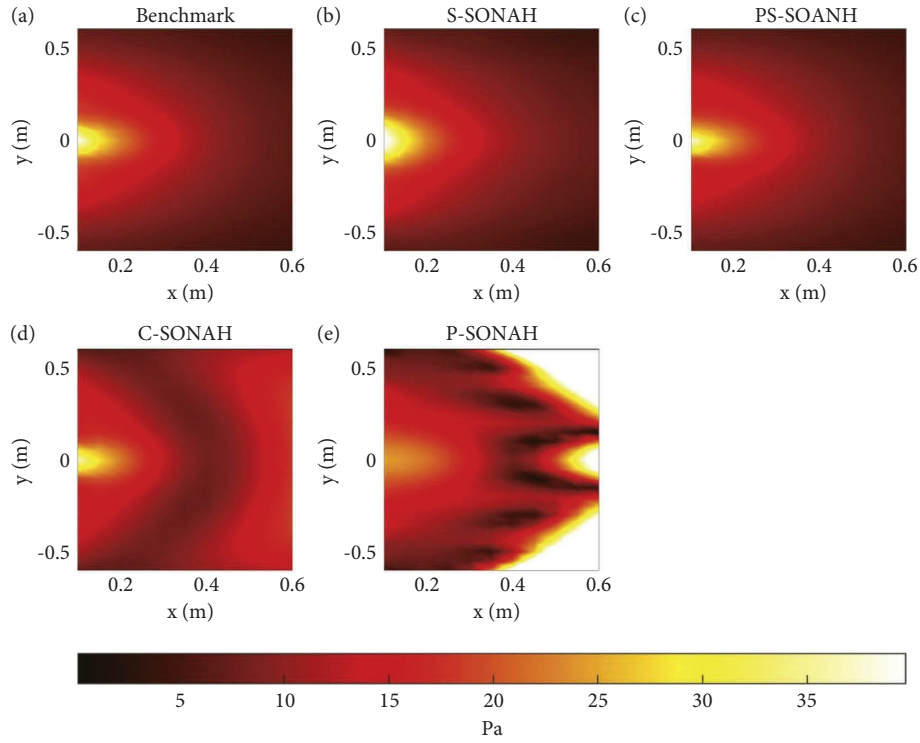

Figure 12: A comparison of the reconstructed pressures at 1000 Hz by S-SONAH, PS-SONAH, C-SONAH, and P-SONAH and the benchmark pressures on the reconstruction surface Γ_3 in terms of a simply supported.

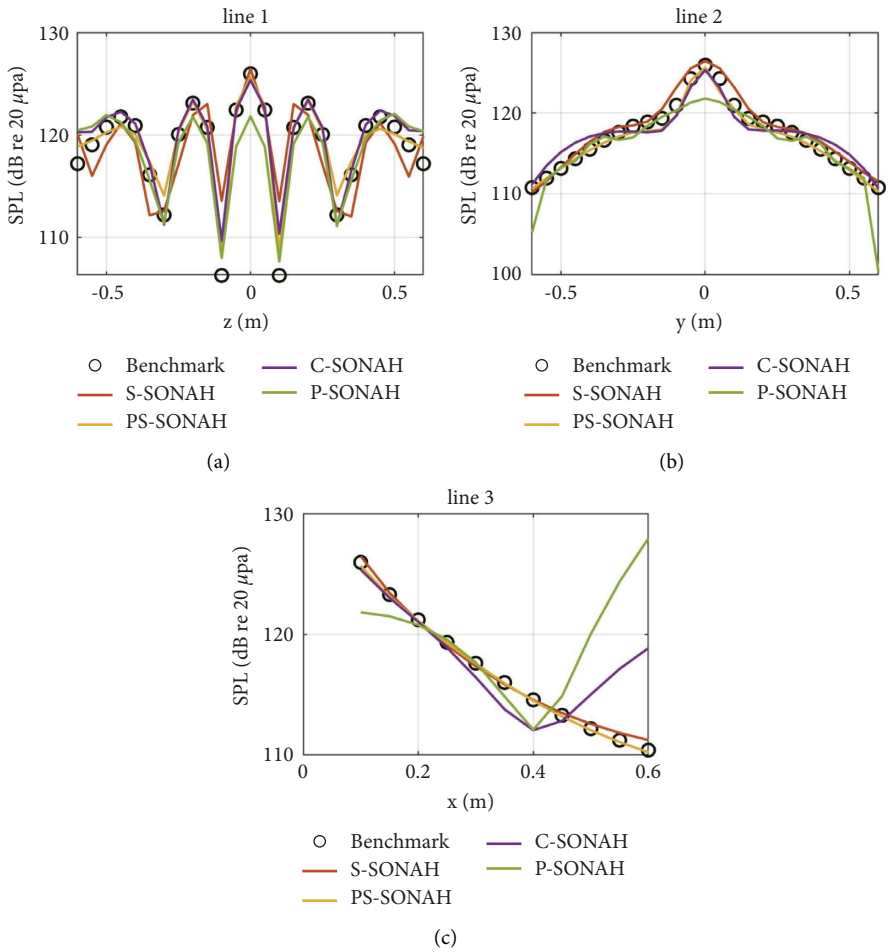

Figure 13: A comparison of the reconstructed SPLs at 1000 Hz by S-SONAH, PS-SONAH, C-SONAH, and P-SONAH and the benchmark SPLs over lines 1–3 in terms of a simply supported thin plate.

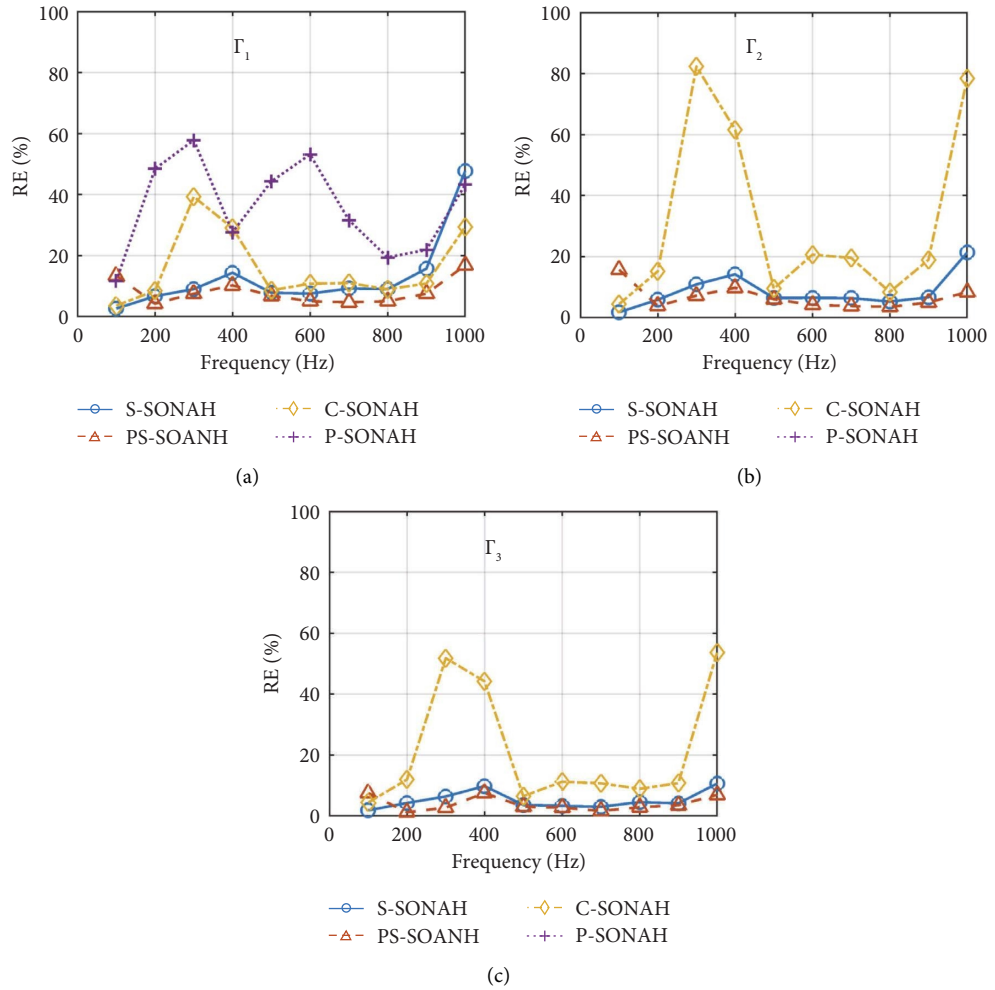

Figure 14: Reconstruction errors of S-SONAH, PS-SONAH, C-SONAH, and P-SONAH on three reconstruction surfaces versus frequency in terms of a simply supported thin plate.

length of the source model $L = 1$ m. Nevertheless, this configuration may not be the most advantageous option and may not yield the most favorable outcomes in terms of sound field reconstruction. To investigate the effect of the interfocal distance on the proposed method's reconstruction results, this section explores different interfocal distances. As shown in Figure 15, different interfocal distances are essentially related to different isosurfaces of the PSWFs. In fact, the interfocal distance controls the size of the isosurfaces and has a significant influence on the ability of the PSWFs to model the sound field. For a given size of sound source or hologram surface, there may exist some guidelines for us to select an appropriate interfocal distance.

The line-array monopoles and simply supported thin plate are employed again in this subsection to examine the performance of PS-SONAH in terms of $d/L = 0.8$, $d/L = 1.0$, and $d/L = 1.2$. The reconstruction errors on surface Γ_1 are shown in Figure 16. It can be seen that RE*s* do not exceed 3% for $d/L = 1.0$ and $d/L = 1.2$ with respect to line-array monopoles. However, RE*s* for $d/L = 0.8$ perform a little higher and grow larger as the frequency increases. As for the simply supported thin plate, RE*s* for $d/L = 0.8$ also present higher values over the entire frequency range. It seems that for elongated sources, when the interfocal distance is larger than the length of the source, better reconstruction results can be ensured. This is because the sound sources are actually singularities in the three-dimensional space and should be incorporated into the singularities of the PSWFs (the line between two focus points). However, the interfocal distance cannot be set too large, as the calculation precision of the PSWFs may decrease [25]. In conclusion, for elongated sound sources, the interfocal distance configuration in PS-SONAH should be slightly larger than the length of the source model ($1.0L$~$1.2L$).

4. Experiment

In order to validate the feasibility of the proposed method, an experimental study is carried out in an anechoic chamber. The photograph of the experimental setup is shown in Figure 17. In the experiment, two bluetooth loudspeakers located at $(0, 0, 0.175)$ m and $(0, 0, -0.175)$ m are used to model an elongated sound source stretched in the z-direction. An identical signal is delivered to both

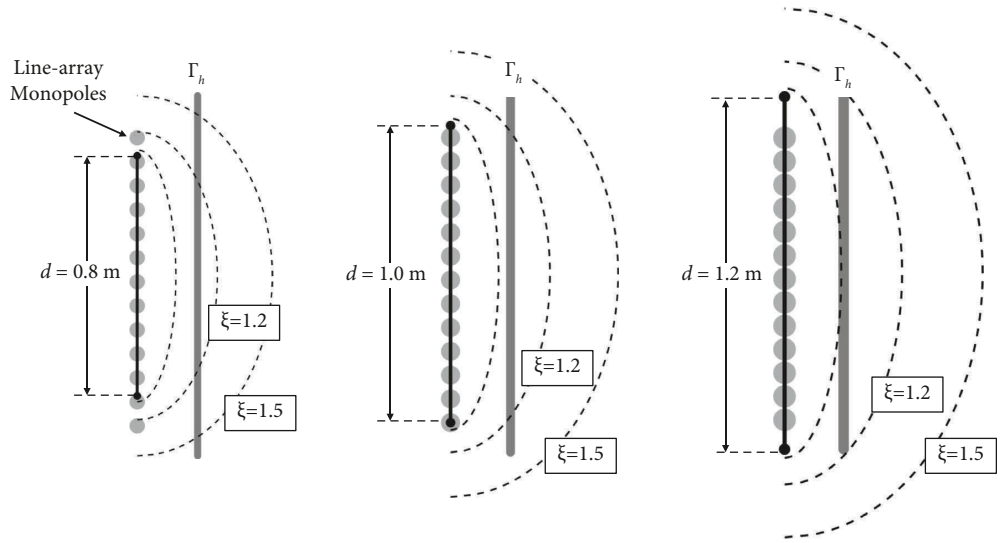

Figure 15: Isosurfaces (dashlines) of the PSWFs for different interfocal distances d.

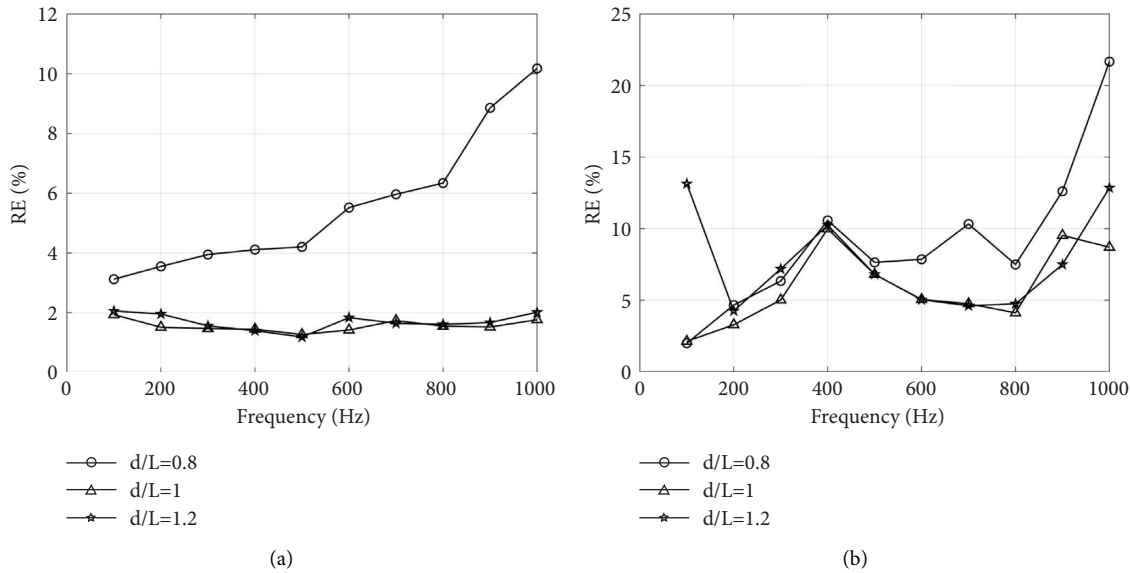

Figure 16: Reconstruction errors of PS-SONAH on surface Γ_1 for different interfocal distances d in terms of (a) line-array monopoles and (b) a simply supported thin plate.

loudspeakers, and they are operated in the same amplitude and phase. The sound pressures are measured by scanning with a planar array of 8×8 microphones. Through a fixed reference microphone, four patch measurements are put together and a total of 256 points are measured. The microphones are distributed uniformly, whose spatial interval is 0.05 m in the y and z directions. The measurements are conducted at 0.2 m (hologram surface Γ_h) and 0.1 m (reconstruction surface Γ_1) away from the loudspeakers. In our experiment, the hologram aperture is set to be large enough in comparison to the size of the sound source model, thereby suppressing the finite measurement aperture effect. Meanwhile, the microphone spacing is set at less than half of the smallest wavelength (0.34 m) across the frequency range (100–1000 Hz), in accordance with the Nyquist–Shannon sampling theorem. In addition, the holography plane offset is set within the smallest wavelength to ensure that evanescent waves can be recorded. However, the measuring configurations are sufficient for the feasibility validation of the proposed method, and the optimization of measurement parameters is not included at this time.

The experiment is first conducted at 1000 Hz to observe the detailed reconstruction results, and the measured pressures at $x = 0.2$ m are shown in Figure 18(a), which are used as input data for different SONAH algorithms. The benchmark pressures at $x = 0.1$ m are shown in Figure 18(b). The circles containing "$*$" represent the locations of two loudspeakers. The origin of the spherical wave functions is set at $(-0.3, 0, 0)$ m. Figure 19 displays the reconstructed pressures by S-SONAH, PS-SONAH, C-

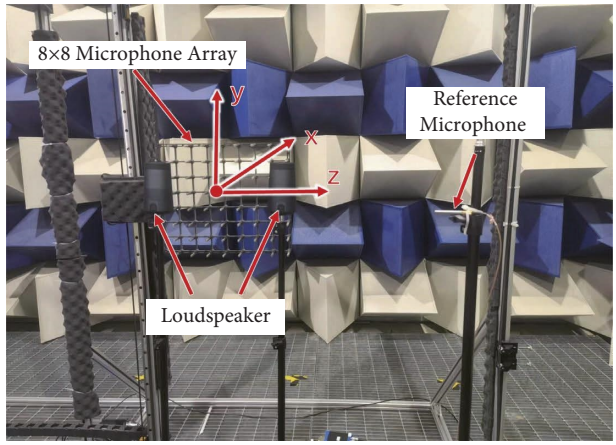

Figure 17: Photograph of the experimental setup.

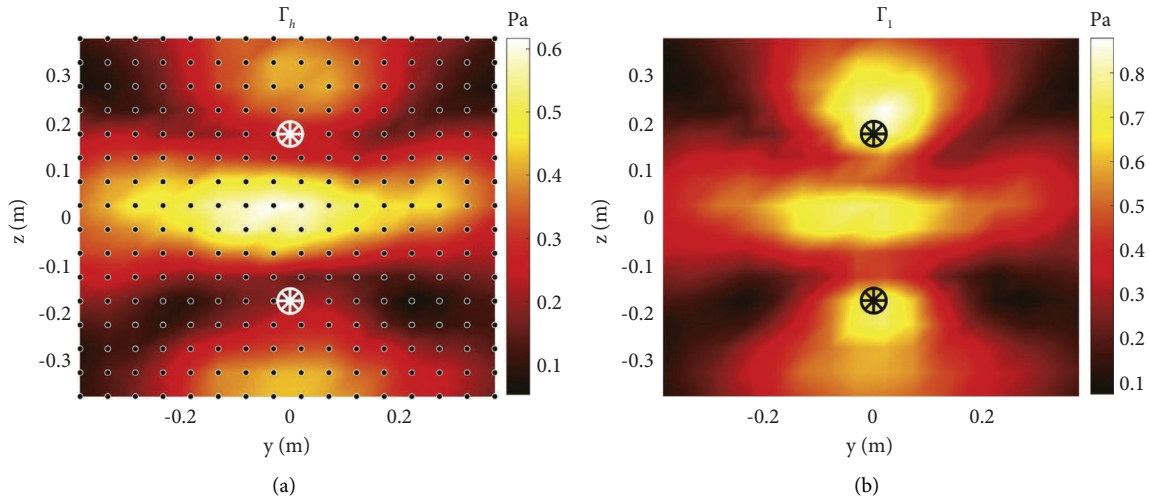

Figure 18: (a) Measured sound pressures on the hologram surface Γ_h at 1000 Hz. The dots represent the sampling measurements, and the circles containing "∗" represent the locations of two loudspeakers. (b) Measured sound pressures (benchmarks) on the reconstruction surface Γ_1.

SONAH, and P-SONAH and the benchmark pressures on surface Γ_1. *REs* of S-SONAH, PS-SONAH, C-SONAH, and P-SONAH on Γ_1 are 34.5%, 32.1%, 30.1%, and 44.2%, respectively. It can be seen that S-SONAH, PS-SONAH, and C-SONAH have similar performances, while the reconstruction error of P-SONAH is a little larger. Figure 20 shows the reconstruction errors versus frequency ranging from 100 Hz to 1000 Hz. As it can be seen, the error curves of S-SONAH, PS-SONAH, and C-SONAH perform similar features across the entire frequency range. Furthermore, the mean REs across the frequency range of S-SONAH, PS-SONAH, and C-SONAH are 25.3%, 22.6%, 27.1%, and 37.4%. Note that the differences among S-SONAH, PS-SONAH, and C-SONAH are not apparent. The reason may be that two loudspeakers are not sufficient to construct a featured elongated sound source model, and the advantages of PS-SONAH for elongated source models cannot be displayed dramatically. However, considering the calculated mean REs, PS-SONAH performs slightly better than S-SONAH and C-SONAH, which demonstrates that PS-SONAH is feasible and effective in practical experiments.

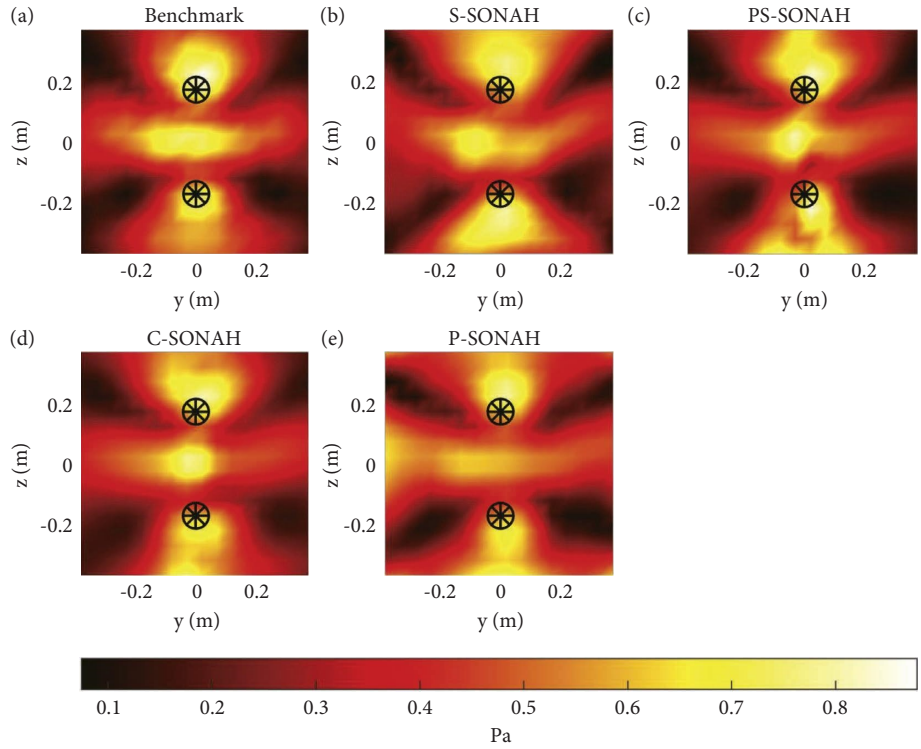

Figure 19: Comparison of the reconstructed pressures at 1000 Hz by S-SONAH, PS-SONAH, C-SONAH, and P-SONAH and the benchmark pressures on the reconstruction surface Γ_1. The circles containing "$*$" represent the locations of two loudspeakers.

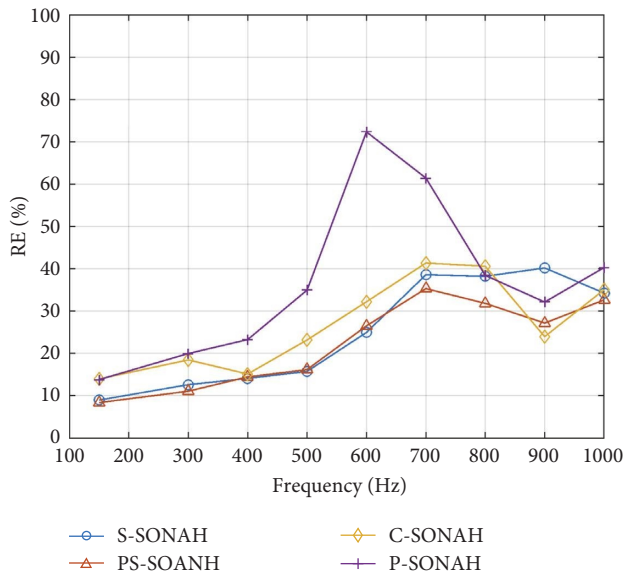

Figure 20: Reconstruction errors of S-SONAH, PS-SONAH, C-SONAH, and P-SONAH on surface Γ_1 versus frequency in terms of two loudspeakers.

5. Conclusions

The successful implementation of NAH is highly related to the appropriate selection or construction of the elementary wave functions (EWFs). If the EWFs can match the characteristics of the sound sources well, fewer expansion terms are required during the sound field projections. As a result, the burden on regularization can be reduced, and the accuracy of the reconstruction results will be improved. In this study, the prolate spheroidal wave functions (PSWFs) are introduced to SONAH, and a proposed method called PS-SONAH is used to reconstruct the radiated sound field of elongated sources. The method represents the sound field as a linear superposition of the PSWFs and establishes

a transfer matrix between the hologram locations and the reconstruction locations. It also combines the modified Tikhonov regularization (MTR) method with the generalized cross validation (GCV) method to stabilize the reconstruction results.

In the numerical simulations and a designed experiment, the proposed method is compared to traditional SONAH algorithms that use plane, cylindrical, or spherical wave functions representing the sound field. The results show that the PS-SONAH method can effectively reconstruct the radiated sound field of elongated sources and performs better reconstruction results. The robustness of the proposed method is validated by the small reconstruction errors across a broad frequency range. Meanwhile, the proposed method is proven applicable to both spatially separated and extended sources. The effect of the interfocal distance on the reconstruction results is also investigated, and a guideline for us to select an appropriate interfocal distance is presented.

Data Availability

The data used to support the findings of this study are available from the corresponding author upon request.

Conflicts of Interest

The authors declare that there are no conflicts of interest regarding the publication of this paper.

Acknowledgments

This work was supported by the National Science Foundation for Distinguished Young Scholars (Grant no. 52201389) and the Natural Science Foundation of Hubei Province of China (Grant no. 2022CFB405).

References

[1] E. G. Williams, *Fourier Acoustics: Sound Radiation and Nearfield Acoustical Holography*, Academic Press, Cambridge, MA, USA, 1999.

[2] W. Cheng, J. Ni, C. Song et al., "Conical statistical optimal near-field acoustic holography with combined regularization," *Sensors*, vol. 21, no. 21, p. 7150, 2021.

[3] A. T. Wall, K. L. Gee, and T. B. Neilsen, "Multisource statistically optimized near-field acoustical holography," *Journal of the Acoustical Society of America*, vol. 137, no. 2, pp. 963–975, 2015.

[4] J. Hald, "Basic theory and properties of statistically optimized near-field acoustical holography," *Journal of the Acoustical Society of America*, vol. 125, no. 4, pp. 2105–2120, 2009.

[5] E. G. Williams and J. D. Maynard, "Holographic imaging without the wavelength resolution limit," *Physical Review Letters*, vol. 45, no. 7, pp. 554–557, 1980.

[6] J. D. Maynard, E. G. Williams, and Y. Lee, "Nearfield acoustic holography: I. Theory of generalized holography and the development of NAH," *Journal of the Acoustical Society of America*, vol. 78, no. 4, pp. 1395–1413, 1985.

[7] I. Lopez Arteaga, R. Scholte, and H. Nijmeijer, "Improved source reconstruction in Fourier-based near-field acoustic holography applied to small apertures," *Mechanical Systems and Signal Processing*, vol. 32, pp. 359–373, 2012.

[8] M. R. Bai, "Application of BEM (boundary element method)-based acoustic holography to radiation analysis of sound sources with arbitrarily shaped geometries," *Journal of the Acoustical Society of America*, vol. 92, no. 1, pp. 533–549, 1992.

[9] Z. W. Luo, D. Fernandez Comesana, C. J. Zheng, and C. X. Bi, "Near-field acoustic holography with three-dimensional scanning measurements," *Journal of Sound and Vibration*, vol. 439, pp. 43–55, 2019.

[10] N. P. Valdivia, "Krylov subspace iterative methods for time domain boundary element method based nearfield acoustical holography," *Journal of Sound and Vibration*, vol. 484, Article ID 115498, 2020.

[11] G. H. Koopmann, L. Song, and J. B. Fahnline, "A method for computing acoustic fields based on the principle of wave superposition," *Journal of the Acoustical Society of America*, vol. 86, no. 6, pp. 2433–2438, 1989.

[12] J. Hald, "Fast wideband acoustical holography," *Journal of the Acoustical Society of America*, vol. 139, no. 4, pp. 1508–1517, 2016.

[13] D.-Y. Hu, H.-B. Li, Y. Hu, and Y. Fang, "Sound field reconstruction with sparse sampling and the equivalent source method," *Mechanical Systems and Signal Processing*, vol. 108, pp. 317–325, 2018.

[14] S. K. Chaitanya and K. Srinivasan, "Equivalent source method based near field acoustic holography using multipath orthogonal matching pursuit," *Applied Acoustics*, vol. 187, Article ID 108501, 2022.

[15] C. Yang, Y. S. Wang, and H. Guo, "Hybrid patch near-field acoustic holography based on Kalman filter," *Applied Acoustics*, vol. 148, pp. 23–33, 2019.

[16] W. Cheng, P. Zhang, C. Song, X. Chen, K. Ou, and M. M. Ahsan, "Resolution enhanced statistically optimal cylindrical near-field acoustic holography based on equivalent source method," *Measurement Science and Technology*, vol. 33, no. 5, Article ID 055015, 2022.

[17] A. Li, J. Chen, J. S. Bolton, Y. Liu, and P. Davies, "Computational statistically optimized near-field acoustical holography (C-SONAH) for virtual noise source identification," *Applied Acoustics*, vol. 203, Article ID 109201, 2023.

[18] Z. Wang and S. F. Wu, "Helmholtz equation–least-squares method for reconstructing the acoustic pressure field," *Journal of the Acoustical Society of America*, vol. 102, no. 4, pp. 2020–2032, 1997.

[19] H. Lu and S. F. Wu, "Reconstruction of vibroacoustic responses of a highly nonspherical structure using Helmholtz equation least-squares method," *Journal of the Acoustical Society of America*, vol. 125, no. 3, pp. 1538–1548, 2009.

[20] L. Jiang, Y. Xiao, and G. Zou, "Data extension near-field acoustic holography based on improved regularization method for resolution enhancement," *Applied Acoustics*, vol. 156, pp. 128–141, 2019.

[21] S. F. Wu, L. Chen, A. Figueroa, and M. Telenko, "Laser-assisted reconstruction of vibro-acoustic behaviors of an arbitrarily shaped vibrating structure," *Journal of Theoretical and Computational Acoustics*, vol. 28, no. 03, Article ID 1950011, 2019.

[22] A. Schuhmacher, J. Hald, K. B. Rasmussen, and P. C. Hansen, "Sound source reconstruction using inverse boundary element calculations," *Journal of the Acoustical Society of America*, vol. 113, no. 1, pp. 114–127, 2003.

[23] Y. Chen, Y. Xiang, Z. Shi, J. Lu, and Y. Wang, "Tikhonov regularized penalty matrix construction method based on the magnitude of singular values and its application in near-field

acoustic holography," *Mechanical Systems and Signal Processing*, vol. 170, Article ID 108870, 2022.
[24] S. F. Wu, *The Helmholtz Equation Least-Squares Method*, Springer, New York, NY, USA, 2015.
[25] C. Flammer, *Spheroidal Wave Functions*, Standford University press, Redwood City, CA, USA, 1957.
[26] L. W. Li, X. K. Kang, and M. S. Leong, *Spheroidal Wave Functions in Electromagnetic Theory*, John Wiley & Sons, Ltd, Hoboken, NJ, USA, 2001.
[27] A. L. Van Buren and J. E. Boisvert, "Accurate calculation of prolate spheroidal radial functions of the first kind and their first derivatives," *Quarterly of Applied Mathematics*, vol. 60, no. 3, pp. 589–599, 2002.
[28] L. W. Li, M. S. Leong, T. S. Yeo, P. S. Kooi, and K. Y. Tan, "Computations of spheroidal harmonics with complex arguments: a review with an algorithm," *Physical Review*, vol. 58, no. 5, pp. 6792–6806, 1998.
[29] P. E. Falloon, P. C. Abbott, and J. B. Wang, "Theory and computation of spheroidal wavefunctions," *Journal of Physics A: Mathematical and General*, vol. 36, no. 20, pp. 5477–5495, 2003.
[30] D. X. Ogburn, C. L. Waters, M. D. Sciffer, J. A. Hogan, and P. C. Abbott, "A finite difference construction of the spheroidal wave functions," *Computer Physics Communications*, vol. 185, no. 1, pp. 244–253, 2014.
[31] R. Adelman, N. A. Gumerov, and R. Duraiswami, "Semi-analytical computation of acoustic scattering by spheroids and disks," *Journal of the Acoustical Society of America*, vol. 136, no. 6, pp. EL405–EL410, 2014.
[32] E. F. Lavia, "Acoustic scattering by two fluid confocal prolate spheroids," *European Journal of Mechanics-B: Fluids*, vol. 88, pp. 47–57, 2021.
[33] Y. Wang, Y. Liu, and J. S. Bolton, "A method to calculate acoustic radiation modes based on spheroidal wave functions," *JASA Express Letters*, vol. 1, no. 1, Article ID 015601, 2021.
[34] P. C. Hansen and D. P. O'Leary, "The use of the L-curve in the regularization of discrete ill-posed problems," *SIAM Journal on Scientific Computing*, vol. 14, no. 6, pp. 1487–1503, 1993.
[35] G. Chertock, "Sound radiation from prolate spheroids," *Journal of the Acoustical Society of America*, vol. 33, no. 7, pp. 871–876, 1961.
[36] J. Hald, "Scaling of plane-wave functions in statistically optimized near-field acoustic holography," *Journal of the Acoustical Society of America*, vol. 136, no. 5, pp. 2687–2696, 2014.
[37] E. G. Williams, "Regularization methods for near-field acoustical holography," *Journal of the Acoustical Society of America*, vol. 110, no. 4, pp. 1976–1988, 2001.